energies

MDPI

Article

Dynamical System Scaling of a Thermocline Thermal Storage System in the Thermal Energy Distribution System (TEDS) Facility

Ramon Yoshiura *,†, Alexander Duenas † and Aaron Epiney

Idaho National Laboratory (INL), 2525 N. Fremont Ave., Idaho Falls, ID 83415, USA; alexander.duenas@inl.gov (A.D.); aaron.epiney@inl.gov (A.E.)
* Correspondence: ramon.yoshiura@inl.gov
† These authors contributed equally to this work.

Abstract: The purpose of this study was to develop a process to convert input signals from one facility into another by reflecting geometric and environmental settings. The Dynamic Energy Transport and Integration Laboratory (DETAIL) is one facility in development that aims to emulate the daily interactions among power production industry systems and be capable of receiving real-time data from those systems as inputs. To convert signals and ensure that the temporal sequences and magnitudes reflect the laboratory settings, the ability to scale and project data is essential. To demonstrate this ability, Dynamical System Scaling (a methodology that enables systems to scale and project or extrapolate datasets to desired environments while conserving the observed transient behavior based on first principles) was applied to DETAIL's thermocline thermal storage system in the Thermal Energy Distribution System. The thermocline system was successfully scaled and a test case was conducted to generate a doubly accelerated energy charge and discharge in reference to past experimental data from the facility. The accelerated data were determined as able to conserve the amount of energy stored and the associated test boundary conditions were charge line maximum temperature, charge line velocity, and thermocline maximum temperature at 354 °C, 0.458 m/s, and 418 °C, respectively. The research results represented a case that required signals to be accelerated without altering the stored energy.

Keywords: integrated energy system;thermal storage system; thermocline thermal storage system; Dynamical System Scaling; design extrapolation; data extrapolation

check for updates

Citation: Yoshiura, R.; Duenas, A.; Epiney, A. Dynamical System Scaling of a Thermocline Thermal Storage System in the Thermal Energy Distribution System (TEDS) Facility. *Energies* **2022**, *15*, 4265. https://doi.org/10.3390/en15124265

Academic Editors: Xiaohu Yang and Kamel Hooman

Received: 9 May 2022
Accepted: 8 June 2022
Published: 10 June 2022

1. Introduction

Integrated energy systems (IESs) are crucial components for maximizing the efficiency of energy usage and complying with growing power demands [1]. The current state of power supply is a superposition of all available power production methodologies, including fossil fuel, nuclear, solar, wind, and others [2]. The coordination of these components is essential to avoid instances of energy waste and outage during emergencies. Recent representative examples of outages and imbalances in grid load were observed in Texas in 2021, when record-breaking low temperatures simultaneously impacted energy production and increased power demand [3], and in Argentina in 2022, when prolonged unexpectedly high temperatures decreased power production efficiency, increased power demand, and eventually affected the supply of quality water as purification systems could not be operated at full capacity [4]. Some of the typical mitigations of these events include temporarily limiting energy usage, importing electricity from neighboring grid operators, utilizing stored energy or load shedding [5]. The role of IESs is to dynamically respond to parameters such as power demand, grid frequency, and grid load balance. At a given time of day, as power usage and power production (especially for renewable energy sources) fluctuates, IESs not only have the potential to regulate power production distribution based on each individual power utility but can also automatically turn on energy storing mechanisms (hydrogen production, thermal storage, etc.) for times of unavoidable cases of excess energy, thereby preventing grid frequency increase [6].

The IES that is represented in the Dynamic Energy Transport and Integration Laboratory (DETAIL) is a combination of thermal storage, battery testing, hydrogen production, electrical vehicle charging, a digital real-time power grid, distributed energy and microgrid, power plant operation, and a non-nuclear microreactor experimental testbed [1]. The goal is to have each system communicate and emulate an IES environment. This includes receiving external signals from industry utilities as inputs to enable real-time data-driven experiments. One component to consider is the design of the experiments when one DETAIL system is interacting with another. Since each facility in DETAIL is an individual specialized group, the physical ties between the systems are uncharted boundaries and for every new experiment design, the integral effects on all systems must be evaluated. Another component to consider is how to translate the industry data into lab configurations. Lab-scale facilities are downscaled versions of industry-scale power plants or energy processing utilities and inputting raw data would not realistically match lab configurations. For this purpose, a data post-processing step is required to convert output data into configurable input data in the correct sequence, based on physics (i.e., when industry-scale data comprise data points for every hour, each data point needs to be converted to correspond to a lab-scale data point).

The purpose of this research was to implement Dynamical System Scaling (DSS) to project, extrapolate or derive initial and boundary conditions, datasets, and new tests based on existing knowledge and generated data from each target application for the facility in question. The DSS methodology is a time-dependent scaling procedure that allows variations in system parameters that are defined by design objectives, the detection of transient distortions, and unique illustrations of generated data [7]. Out of the numerous capabilities provided by DSS, the data synthesis and scaling analysis tools are of particular interest. The utilization of both tools grants users the ability to analyze critical data, considering first- and second-order effects, and the mathematical algorithms to perform such activities are codable.

One example of using the DSS scaling analysis tools to engineer components is the optimization of the core makeup tank (CMT) from Westinghouse AP1000, which was simulated via RELAP5-3D [8]. Using developed DSS code in RAVEN, the CMT was downscaled in size while maintaining the same draining time. Another example is the downscaling of the Experimental Breeder Reactor-II metallic fuel rods to shorten the required irradiation time [9]. Based on neutronics, reactor physics, and thermohydraulics, the fuel rod geometry for the desired irradiation time was determined. The application of DSS and other modern scaling techniques to systems and models that are developed under the integrated energy system (IES) program constitutes a logical continuation of previous IES work, in which systems were analyzed using traditional scaling approaches [10].

To apply the test extrapolation case, our research team selected a thermocline thermal storage system (TTSS) in the Thermal Energy Distribution System (TEDS) facility of the Idaho National Laboratory (INL), which is part of DETAIL under the IES program. One of the missions of the IES program is to optimize thermodynamic and financial efficiency through system integration [11]. The TEDS facility was designed to demonstrate thermal system functions for the generation, storage, delivery, and use of high-quality energy products to support industrial processes and grid infrastructure [12]. Through the modulation of flow rate and heat input, which are controlled by electrical heaters to emulate the steam from nuclear power plants (NPPs), thermal energy is transferred to heat storage systems or heat customers. This functionality is beneficial for NPPs since the most efficient and economic mode of operation is constant thermal power. When the energy demand requires a ramp-down in power from an NPP, it is unlikely that procedures would be initiated for power adjustments due to possible safety and economic repercussions. The ability to store or sell thermal energy is one way to deal with excess energy production while meeting energy demand.

Currently, the validation activity for the TEDS model is being conducted in Dymola (Modelica-based) with collected TEDS facility data [13]. The simulation covers transient physics-based models for scaled-up IESs, including NPP designs from Westinghouse and NuScale Power. Coupling reactor modules with heat transfer loops to test the feasibility of heat extraction from NPPs requires the simulation of the system performance in advance. The simulation must be capable of reproducing experimental results. Therefore, a set of representative experiments need to be defined and used to validate the models against experimental results. For validation cases, such as that of TEDS, the current research focused on projecting data and the required operational conditions to accelerate the charge and discharge process of a TTSS as a potential future test design that could support code validation.

2. Materials and Methods

2.1. TEDS Overview

The TEDS facility is one of the energy storage systems in DETAIL, which specializes in thermal charge, storage, and discharge. It comprises the following seven components: a therminol tank, oil–glycol heat exchanger (HX), filtration system, driving pump, heat injection system, TTSS, and therminol regulation system (as shown in Figures 1 and 2 [11]).

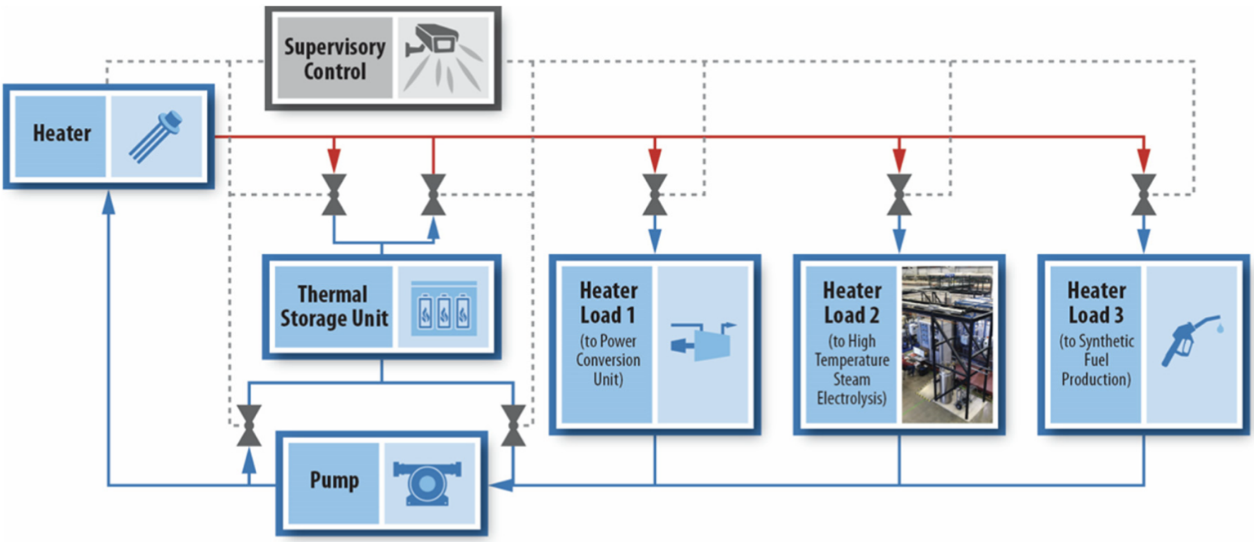

Figure 1. A TEDS schematic [11].

Starting from the tank repository, therminol 66 (the fluid used to transport heat) is driven through the heat injection system, which consists of a heat source HX and a Chromalox heater to ramp up the fluid temperature, to transfer the desired amount of heat to the TTSS. Both heat supply systems are installed to allow TEDS to run in DETAIL in dependent or independent mode. The dependent mode physically injects heated fluid from other DETAIL facilities into the heat source HX whereas independent mode generates heat from the Chromalox heater. As previously mentioned, DETAIL is a multicomponent integrated system that connects power grids to energy storage systems, electrical utilization, distributed microgrids, and other infrastructures that are built within or outside of INL [1]. When in-house or external real-time heat output data are provided as digital signals, the output signals are used as time-dependent inputs to regulate the Chromalox heater and emulate real-time heat storage. To demonstrate this capability with reference to normal and emergency grid operations, the INL real-time power simulation test platform and the TEDS networks were connected to be tested. The anticipated external heat output sources were renewable energy, fossil fuel power, nuclear power, and other possible industrial processes that produce excess heat. The generated TEDS data could also serve as a data source to validate models in transient physics-based models that simulate the interactions between hybrid energy systems and nuclear power plants.

Figure 2. A picture of TEDS with a heat exchanger.

2.2. Dynamical System Scaling

The DSS approach to system scaling is based on transforming the typical view of a process into a special coordinated system in terms of the parameter of interest and its agents of change [14]. By parameterizing a process using a time term, which is introduced later in this section, the reproduced data can be converted into the special three-coordinate system (also called the phase space) and form a geometry with curves along the surface that contain invariant and intrinsic properties. The remainder of this section is a review of DSS theory, which was introduced into publications by Reyes [7,14,15] and was used in this analysis for the thermocline scaling. The parameter of interest is defined as a conserved quantity within a control volume:

$$\beta(t) = \frac{1}{\Psi_0} \iiint_V \psi(\vec{x}, t) dV \tag{1}$$

where β is defined as the volume integral of the time- and space-dependent conserved quantity ψ when normalized by a time-independent value Ψ_0, which characterizes the process. The agents of change are defined as the first derivative of the normalized parameter of interest:

$$\omega = \frac{1}{\Psi_0} \frac{d}{dt} \iiint_V \psi(\vec{x}, t) dV = \iiint_V \left(\phi_v + \phi_f\right) dV + \iint_A \left(\vec{j} \cdot \vec{n}\right) dA - \iint_A \psi(\vec{v} - \vec{v}_s \cdot \vec{n} dA) dA \tag{2}$$

The changes are categorized into three components: volumetric, surface, and quantity transport. The agents of change are also the sum of the individual agents of change:

$$\omega = \frac{1}{\Psi_0} \frac{d}{dt} \iiint_V \psi(\vec{x}, t) dV = \sum_{i=1}^{n} \omega_i \tag{3}$$

The relationship between ω and β is the following:

$$\omega(t) = \left. \frac{d\beta}{dt} \right|_t = \sum_{i=1}^{n} \omega_i \tag{4}$$

where ω is the first derivative of the reference time. As defined in Einstein and Infeld, time is a value that moves in constant increments [16]. The process-dependent term in DSS is called process time:

$$\tau(t) = \frac{\beta(t)}{\omega(t)} \tag{5}$$

To measure the progression difference between the reference time and process time in terms of the reference time, the idea of temporal displacement rate (D) is adopted:

$$D = \frac{d\tau - dt}{dt} = -\frac{\beta}{\omega^2} \frac{d\omega}{dt} \tag{6}$$

The interval of the process time is:

$$d\tau = \tau_s = (1 + D)dt \tag{7}$$

Applying the process action to normalize the phase space coordinates produces the following normalized terms:

$$\tilde{\Omega} = \omega \tau_s, \qquad \tilde{\beta} = \beta, \qquad \tilde{t} = \frac{t}{\tau_s}, \qquad \tilde{\tau} = \frac{\tau}{\tau_s}, \qquad \tilde{D} = D \tag{8}$$

The scaling relationship between the prototype and model can be defined for both β and ω and represents the scaling of the parameter of interest and its corresponding agents of change (or the frequency obtained from the units of time):

$$\lambda_A = \frac{\beta_M}{\beta_P}, \qquad \lambda_B = \frac{\omega_M}{\omega_P} \tag{9}$$

where the subscripts M and P stand for the model and prototype, respectively. The application of these scaling ratios to Equations (5), (6), and (8) provides the scaling ratios for other parameters as well:

$$\frac{t_M}{t_P} = \frac{\lambda_A}{\lambda_B}, \qquad \frac{\tau_M}{\tau_P} = \frac{\lambda_A}{\lambda_B}, \qquad \frac{\tilde{\beta}_M}{\tilde{\beta}_P} = \lambda_A, \qquad \frac{\tilde{\Omega}_M}{\tilde{\Omega}_P} = \lambda_A, \qquad \frac{\tilde{\tau}_M}{\tilde{\tau}_P} = 1, \qquad \frac{D_M}{D_P} = 1 \tag{10}$$

The normalized agent of change is the sum in the same respect:

$$\Omega = \sum_{i=1}^{k} \Omega_i \tag{11}$$

The ratio of Ω is expressed in the following alternative form:

$$\Omega_R = \frac{\Omega_M}{\Omega_P} = \frac{\sum_{i=1}^{k} \Omega_{M,i}}{\sum_{i=1}^{k} \Omega_{P,i}} = \frac{\Omega_{M,1} + \Omega_{M,2} + \ldots + \Omega_{M,k}}{\Omega_{P,1} + \Omega_{P,2} + \ldots + \Omega_{P,k}} \tag{12}$$

By the law of scaling ratios, the following must be true:

$$\lambda_A = \frac{\Omega_{M,1}}{\Omega_{P,1}}, \lambda_A = \frac{\Omega_{M,2}}{\Omega_{P,2}}, \ldots, \lambda_A = \frac{\Omega_{M,k}}{\Omega_{P,k}} \tag{13}$$

3. Thermal Energy Distribution System–Thermocline Thermal Storage System Equation Scaling

The TTSS sits between the hot and cold lines that allow flows from either section, depending on the operation mode [11]. The following sections characterize the conversation rules and non-dimensionalize the process when necessary.

3.1. Mass Flow Rate

When the mass flow rate from the inlet is m, then by conservation of mass, the mass flow rate within the TTSS must be the equivalent:

$$\dot{m} = \rho_{in} v_{z,in} \pi R_{in}^2 = \rho_{th} v_{z,th} \varepsilon \pi R_{th}^2 \quad (14)$$

where ρ_{in} is the inlet density, ρ_{th} is the TTSS density, $v_{z,in}$ is the inlet axial velocity, $v_{z,th}$ is the TTSS axial velocity, R_{in} is the inlet pipe radius, ε is the porosity (ratio of fluid to filler), and R_{th} is the TTSS fluid tank radius. The TTSS axial velocity is the following:

$$v_{z,th} = \frac{\rho_{in} R_{in}^2 v_{z,in}}{\rho_{th} \varepsilon R_{th}^2} \quad (15)$$

3.2. Conservation of Mass

In cylindrical coordinates, the compressible conservation of mass is:

$$\frac{\partial \rho_{th}}{\partial t} + \frac{1}{r}\frac{\partial(\rho_{th} r v_{r,th})}{\partial r} + \frac{v_{\theta,th}}{r}\frac{\partial(\rho_{th} v_{\theta,th})}{\partial \theta} + \frac{\partial v_{z,th}}{\partial z} = 0 \quad (16)$$

where $v_{r,th}$ is the TTSS radial velocity and $v_{\theta,th}$ is the TTSS azimuthal velocity. By expanding the terms and ignoring the radial and azimuthal velocities, the differential density is:

$$\frac{\partial \rho_{th}}{\partial t} = -v_z \frac{\partial \rho_{th}}{\partial z} - \rho_{th}\frac{\partial v_z}{\partial z} \quad (17)$$

3.3. Conservation of Momentum

In cylindrical coordinates, the compressible conservation of momentum in the axial direction is:

$$\frac{D(\rho_{th} v_{z,th})}{Dt} = -\frac{\partial P}{\partial z} + \mu_{th}\left(\frac{1}{r}\frac{\partial}{\partial r}\left[r\frac{\partial v_{z,th}}{\partial r}\right] + \frac{1}{r^2}\frac{\partial^2 v_{z,th}}{\partial \theta^2} + \frac{\partial^2 v_{z,th}}{\partial z^2}\right) \quad (18)$$

where P is the TTSS internal pressure. By expanding the terms, the differential axial velocity is:

$$\frac{\partial v_{z,th}}{\partial t} = -\frac{v_{z,th}}{\rho_{th}}\frac{\partial \rho_{th}}{\partial t} - \frac{1}{\rho_{th}}\frac{\partial P}{\partial z} + \nu\left(\frac{1}{r}\frac{\partial v_{z,th}}{\partial r} + \frac{\partial^2 v_{z,th}}{\partial r^2} + \frac{\partial^2 v_{z,th}}{\partial z^2}\right) \quad (19)$$

3.4. Conservation of Energy

From Konor et al. [11], the thermocline heat transfer equation that characterizes the energy conservation of a fluid flow through porous media for low- and no-flows is (originally from Gunn (1978) [17] and modified in [18]):

$$\rho_{th} c_{P,th} \varepsilon \pi R_{th}^2 dz \frac{\partial T_{th}}{\partial t} = \rho_{th} \varepsilon \pi R_{th}^2 v_{z,th}(h_z - h_{z+dz}) + h_c S_r \left(T_{fr} - T_{th}\right) dz + \dot{Q}_{losses} \quad (20)$$

where ε is the porosity, h_z is the specific enthalpy of the current node, h_{z+dz} is the specific enthalpy of the next axial node, h_c is the convective heat transfer coefficient between the fluid and filler, S_{fr} is the heat transfer area of filler per unit length of the tank, T_{fr} is the filler temperature, T_{th} is the TTSS fluid temperature, dz is the axial distance between each node, and $\dot{Q}_{losses}$ is the heat conduction through the walls. When the specific enthalpy is replaced by the specific heat and temperature at the node, the heat transfer equation is:

$$\begin{aligned} \rho_{th} c_{P,th} \varepsilon \pi R_{th}^2 dz \frac{\partial T_{th}}{\partial t} &= \rho_{th} \varepsilon \pi R_{th}^2 v_{z,th} \left(c_{P,z,th} T_{th,z} - c_{P,z+dz,th} T_{th,z+dz} \right) \\ &\quad + h_c S_r \left(T_{fr} - T_{th} \right) dz + \dot{Q}_{losses} \end{aligned} \tag{21}$$

By dividing both sides by dz and considering the specific enthalpy difference portion as a form of first-order forward numeric differentiation, the difference can be rewritten as the spatial first derivative of the specific enthalpy in the axial direction:

$$\rho_{th} c_{P,th} \varepsilon \pi R_{th}^2 \frac{\partial T_{th}}{\partial t} = \rho_{th} \varepsilon \pi R_{th}^2 v_{z,th} \frac{\partial (c_{P,th} T_{th})}{\partial z} + h_c S_r \left(T_{fr} - T_{th} \right) + \frac{\dot{Q}_{losses}}{dz} \tag{22}$$

By using Equation (15) for the TTSS axial velocity and expanding the terms, it can be reorganized as:

$$\frac{\partial T_{th}}{\partial t} = \frac{\rho_{in} R_{in}^2 v_{z,in}}{\rho_{th} c_{P,th} R_{th}^2} \left(T_{th} \frac{\partial c_{P,th}}{\partial z} + c_{P,th} \frac{\partial T_{th}}{\partial z} \right) + \frac{h_c S_r \left(T_{fr} - T_{th} \right)}{\rho_{th} c_{P,th} \varepsilon \pi R_{th}^2} + \frac{\dot{Q}_{losses}}{\rho_{th} c_{P,th} \varepsilon \pi R_{th}^2 dz} \tag{23}$$

The wall losses can be expressed by representing the heat transfer radially across the wall to the outer ambient air:

$$\begin{aligned} \frac{\partial T_{th}}{\partial t} &= \frac{\rho_{in} R_{in}^2 v_{z,in}}{\rho_{th} c_{P,th} R_{th}^2} \left(T_{th} \frac{\partial c_{P,th}}{\partial z} + c_{P,th} \frac{\partial T_{th}}{\partial z} \right) + \frac{h_c S_r \left(T_{fr} - T_{th} \right)}{\rho_{th} c_{P,th} \varepsilon \pi R_{th}^2} \\ &\quad + \frac{\pi R_w^2}{\rho_{th} c_{P,th} \varepsilon \pi R_{th}^2} \left(\frac{k}{r} \frac{\partial T_w}{\partial r} + \frac{\partial k}{\partial r} \frac{\partial T_w}{\partial r} + k \frac{\partial^2 T_w}{\partial r^2} \right) \end{aligned} \tag{24}$$

where T_w is the wall temperature.

3.5. System Discretization

The key is to consider which node represents the entire TTSS, including the inlet, outlet, and wall nodes. For this study, the central mid-axial node was selected. It is assumed that the first derivatives in the advective term are an nth-order central numerical discretization in the axial direction that spanned from the inlet to the outlet and that Δz is a sufficiently small uniform grid. Then, Equation (24) changes to:

$$\begin{aligned} \frac{\partial T_{th}}{\partial t} &= \frac{\rho_{in} R_{in}^2 v_{z,in}}{\rho_{th} c_{P,th} R_{th}^2} \left(T_{th} \left[\frac{\pm A_{i-n/2} c_{P,th,i-n/2} \mp \cdots \mp A_{i+n/2} c_{P,th,i+n/2}}{\Delta z} \right] \right. \\ &\quad \left. + c_{P,th} \left[\frac{\pm A_{i-n/2} T_{th,i-n/2} \mp \cdots \mp A_{i+n/2} T_{th,i+n/2}}{\Delta z} \right] \right) + \frac{h_c S_r \left(T_{fr} - T_{th} \right)}{\rho_{th} c_{P,th} \varepsilon \pi R_{th}^2} \\ &\quad + \frac{R_w^2}{\rho_{th} c_{P,th} \varepsilon R_{th}^2} \left(\frac{k}{r} \frac{\partial T_w}{\partial r} + \frac{\partial k}{\partial r} \frac{\partial T_w}{\partial r} + k \frac{\partial^2 T_w}{\partial r^2} \right) \end{aligned}$$

where A is the coefficient of the corresponding nth-order central discretization and the end points at nodes $i - n/2$ and $i + n/2$ are the inlet and outlet, respectively. Similarly, the wall radial discretization can be mth-order forwarding with Δr as the uniform radial spacing:

$$\begin{aligned}\frac{\partial T_{th}}{\partial t} &= \frac{\rho_{in} R_{in}^2 v_{z,in}}{\rho_{th} c_{P,th} R_{th}^2}\left(T_{th}\left[\frac{\pm A_{i-n/2} c_{P,in} \mp \cdots \mp A_{i+n/2} c_{P,out}}{\Delta z}\right]\right. \\ &\quad \left. + c_{P,th}\left[\frac{\pm A_{i-n/2} T_{in} \mp \cdots \mp A_{i+n/2} T_{out}}{\Delta z}\right]\right) + \frac{h_c S_r \left(T_{fr} - T_{th}\right)}{\rho_{th} c_{P,th} \varepsilon \pi R_{th}^2} \\ &\quad + \frac{R_w^2}{\rho_{th} c_{P,th} \varepsilon \pi R_{th}^2}\left(\frac{k}{r}\left[\frac{\pm B_{i,j} T_{w,i,j} \mp \cdots \pm B_{i,j+m} T_{w,i,j+m}}{\Delta r}\right]\right. \\ &\quad + \left[\frac{\pm B_{i,j} k_{i,j} \mp \cdots \pm B_{i,j+m} k_{i,j+m}}{\Delta r}\right]\left[\frac{\pm B_{i,j} T_{w,i,j} \mp \cdots \pm B_{i,j+m} T_{w,i,j+m}}{\Delta r}\right] \\ &\quad \left. + k\left[\frac{\pm C_{i,j} T_{w,i,j} \mp \cdots \pm C_{i,j+m} T_{w,i,j+m}}{\Delta r^2}\right]\right)\end{aligned} \tag{25}$$

where nodes (i, j) and $(i, j + m)$ are the inner wall and outer ambient locations, respectively.

3.6. Non-Dimensionlization

The TTSS fluid temperature T_{th}, inlet fluid temperature T_{in}, outlet fluid temperature T_{out}, inner wall temperature $T_{i,j} = T_w$, outer ambient temperature $T_{i,j+m} = T_{amb}$, and inlet velocity $v_{z,in}$ are variables that are available from TEDS data. These variables are non-dimensionlizable in the following form:

$$T_{th}^+ = \frac{T_{th}}{T_{th,0}}, T_{in}^+ = \frac{T_{in}}{T_{in,0}}, T_{out}^+ = \frac{T_{out}}{T_{out,0}}, T_w^+ = \frac{T_w}{T_{w,0}}, T_{amb}^+ = \frac{T_{amb}}{T_{amb,0}}, v_{z,in}^+ = \frac{v_{z,in}}{T_{z,in,0}} \tag{26}$$

Using Equations (27) and (28), the conservation of energy can be successfully non-dimensionlized to satisfy the DSS requirements:

$$\begin{aligned}\frac{\partial T_{th}^+}{\partial t} &= \frac{\rho_{in} R_{in}^2 v_{z,in,0} v_{z,in}^+}{\rho_{th} c_{P,th} R_{th}^2}\left(T_{th}^+\left[\frac{\pm A_{i-n/2} c_{P,in} \mp \cdots \mp A_{i+n/2} c_{P,out}}{\Delta z}\right]\right. \\ &\quad \left. \pm \frac{A_{i-n/2} c_{P,th} T_{in,0} T_{in}^+}{\Delta z T_{th,0}} \mp \frac{c_{P,th}}{T_{th,0}} \frac{\cdots}{\Delta z} \mp \frac{A_{i+n/2} c_{P,th} T_{out,0} T_{out}^+}{\Delta z T_{th,0}}\right) + \frac{h_c S_r \left(T_{fr} - T_{th}\right)}{\rho_{th} c_{P,th} \varepsilon \pi R_{th}^2 T_{th,0}} \\ &\quad + \frac{R_w^2}{\rho_{th} c_{P,th} \varepsilon \pi R_{th}^2 T_{th,0}}\left(\frac{k}{r\Delta r}\left[\pm B_{i,j} T_w T_w^+ \mp \cdots \pm B_{i,j+m} T_{amb,0} T_{amb}^+\right]\right. \\ &\quad + \left[\frac{\pm B_{i,j} k_{i,j} \mp \cdots \pm B_{i,j+m} k_{i,j+m}}{\Delta r}\right]\left[\frac{\pm B_{i,j} T_{w,0} T_w^+ \mp \cdots \pm B_{i,j+m} T_{amb,0} T_{amb}^+}{\Delta r}\right] \\ &\quad \left. + k\left[\frac{\pm C_{i,j} T_{w,0} T_w^+ \mp \cdots \pm C_{i,j+m} T_{amb,0} T_{amb}^+}{\Delta r^2}\right]\right)\end{aligned} \tag{27}$$

As described in Equation (9), the ratio between the parameters of interest and agents of change for the model and the prototype are $\lambda_A = \frac{\beta_M}{\beta_P}$ and $\lambda_B = \frac{\omega_M}{\omega_P}$. The scaling ratios for the given non-dimensionalized variables are the following:

$$\begin{aligned}&\lambda_{A,th} = \frac{T_{th,M}}{T_{th,P}}, \lambda_{B,th} = \frac{\left.\frac{\partial T_{th}}{\partial t}\cdot\right|_M}{\left.\frac{\partial T_{th}}{\partial t}\right|_P}, \lambda_{A,v_{z,in}} = \frac{v_{z,in,M}}{v_{z,in,P}}, \lambda_{B,v_{z,in}} = \frac{\left.\frac{\partial v_{z,in}}{\partial t}\cdot\right|_M}{\left.\frac{\partial v_{z,in}}{\partial t}\right|_P}, \\ &\lambda_{A,T_{in}} = \frac{T_{in,M}}{T_{in,P}}, \lambda_{B,T_{in}} = \frac{\left.\frac{\partial T_{in}}{\partial t}\cdot\right|_M}{\left.\frac{\partial T_{in}}{\partial t}\right|_P}, \lambda_{A,T_{out}} = \frac{T_{out,M}}{T_{out,P}}, \lambda_{B,T_{out}} = \frac{\left.\frac{\partial T_{out}}{\partial t}\cdot\right|_M}{\left.\frac{\partial T_{out}}{\partial t}\right|_P} \\ &\lambda_{A,T_w} = \frac{T_{w,M}}{T_{w,P}}, \lambda_{B,T_w} = \frac{\left.\frac{\partial T_w}{\partial t}\cdot\right|_M}{\left.\frac{\partial T_w}{\partial t}\right|_P}, \lambda_{A,T_{amb}} = \frac{T_{amb,M}}{T_{amb,P}}, \lambda_{B,T_{amb}} = \frac{\left.\frac{\partial T_{amb}}{\partial t}\cdot\right|_M}{\left.\frac{\partial T_{amb}}{\partial t}\right|_P}\end{aligned} \tag{28}$$

However, each set of scaling ratios shares the same global time ratio:

$$t_R = \frac{t_M}{t_P} = \frac{\lambda_{A,th}}{\lambda_{B,th}} = \frac{\lambda_{A,v_{z,in}}}{\lambda_{B,v_{z,in}}} = \frac{\lambda_{A,T_{in}}}{\lambda_{B,T_{in}}} = \frac{\lambda_{A,T_{out}}}{\lambda_{B,T_{out}}} = \frac{\lambda_{A,T_w}}{\lambda_{B,T_w}} = \frac{\lambda_{A,T_{amb}}}{\lambda_{B,T_{amb}}} \tag{29}$$

3.7. Law of Scaling Ratio

By applying the law of scaled ratios (as described in Equation (13)) and non-dimensionalized variables, the following relations are true:

$$\begin{aligned}
\lambda_{A,v_{z,in}} &= \left(\frac{\rho_{th} c_{P,th} R_{th}^2 \Delta z}{\rho_{in} c_{P,in} R_{in}^2 \varepsilon v_{z,in,0}}\right)_R t_R \\
\lambda_{A,T_{in}} &= \left(\frac{T_{th,0} c_{P,in}}{T_{in,0} c_{P,th}}\right)_R \lambda_{A,th}, \lambda_{B,T_{in}} = \left(\frac{T_{th,0} c_{P,in}}{T_{in,0} c_{P,th}}\right)_R \frac{\lambda_{A,th}}{t_R} \\
\lambda_{A,T_{out}} &= \left(\frac{T_{th,0} c_{P,out}}{T_{out,0} c_{P,th}}\right)_R \lambda_{A,th}, \lambda_{B,T_{out}} = \left(\frac{T_{th,0} c_{P,out}}{T_{out,0} c_{P,th}}\right)_R \frac{\lambda_{A,th}}{t_R} \\
\lambda_{A,T_w} &= \left(\frac{\rho_{th} c_{P,th} R_{th}^2 \varepsilon r \Delta r T_{th,0}}{R_w^2 k T_{w,0}}\right)_R t_R \lambda_{A,th}, \lambda_{B,T_w} = \left(\frac{\rho_{th} c_{P,th} R_{th}^2 \varepsilon r \Delta r T_{th,0}}{R_w^2 k T_{w,0}}\right)_R \lambda_{A,th} \\
\lambda_{A,T_{amb}} &= \left(\frac{\rho_{th} c_{P,th} R_{th}^2 \varepsilon r \Delta r T_{th,0}}{R_w^2 k T_{amb,0}}\right)_R t_R \lambda_{A,th}, \lambda_{B,T_{amb}} = \left(\frac{\rho_{th} c_{P,th} R_{th}^2 \varepsilon r \Delta r T_{th,0}}{R_w^2 k T_{amb,0}}\right)_R \lambda_{A,th}
\end{aligned} \tag{30}$$

Assuming the ambient temperature remains the same in both the model and the prototype, the scaling ratio is $\lambda_{T_{amb}} = 1$. Thus, the scaling ratio for the TTSS fluid temperature is:

$$\lambda_{A,th} = \left(\frac{R_w^2 k T_{amb}}{\rho_{th} c_{P,th} R_{th}^2 \varepsilon r \Delta r T_{th,0}}\right)_R \frac{1}{t_R} \tag{31}$$

The terms in Equation (31) can then be replaced with the scaling ratios in Equation (30). Recall that geometry and material changes are not accepted $(T_{amb,0,R} = \Delta r_R = \Delta z_R = r_R = R_{th,R} = \epsilon_R = 1)$. To maintain mechanical flow conditions, the inlet velocity nominal value must be identical $(v_{z,in,0,R} = 1)$:

$$\begin{aligned}
\lambda_{A,th} &= \left(\frac{k}{\rho_{th} c_{P,th} T_{th,0}}\right) \frac{1}{t_R} \\
\lambda_{A,v_{z,in}} &= \left(\frac{\rho_{th} c_{P,th}}{\rho_{in} c_{P,in}}\right)_R t_R, \lambda_{B,v_{z,in}} = \left(\frac{\rho_{th} c_{P,th}}{\rho_{in} c_{P,in}}\right)_R \\
\lambda_{A,T_{in}} &= \left(\frac{c_{P,in} k}{\rho_{th} c_{P,th}^2 T_{in,0}}\right)_R \frac{1}{t_R}, \lambda_{B,T_{in}} = \left(\frac{c_{P,in} k}{\rho_{th} c_{P,th}^2 T_{in,0}}\right)_R \frac{1}{t_R^2} \\
\lambda_{A,T_{out}} &= \left(\frac{c_{P,out} k}{\rho_{th} c_{P,th}^2 T_{out,0}}\right)_R \frac{1}{t_R}, \lambda_{B,T_{out}} = \left(\frac{c_{P,out} k}{\rho_{th} c_{P,th}^2 T_{out,0}}\right)_R \frac{1}{t_R^2} \\
\lambda_{A,T_w} &= \left(\frac{1}{T_{w,0}}\right)_R, \lambda_{B,T_w} = \left(\frac{1}{T_{w,0}}\right)_R \frac{1}{t_R}
\end{aligned} \tag{32}$$

3.8. DSS Scaling Type Application

From Reyes, the scaling methods and similarity criteria are subdivided into five categories: 2–2 affine, dilation, β-strain, ω-strain, and identity [14]. Table 1 summarizes the similarity criteria. Despite the five categories, in essence, all are 2–2 affines, with the exception of the partial scaling ratio values being 1.

Table 1. Scaling methods and similarity criteria that result from two-parameter transformations [14].

Basis for Process Space–Time Coordinate Scaling				
Metric Invariance	$d\tilde{\tau}_P = d\tilde{\tau}_P$	and	Covariance Principle	$\frac{1}{\omega_P}\frac{d\beta_P}{dt_P} = \frac{1}{\omega_M}\frac{d\beta_M}{dt_M}$
$\beta - \omega$ Coordinate Transformations				
2–2 Affine $\beta_R = \lambda_A$ $\omega_R = \lambda_B$	Dilation $\beta_R = \lambda$ $\omega_R = \lambda$	β-Strain $\beta_R = \lambda_A$ $\omega_R = 1$	ω-Strain $\beta_R = 1 = \lambda_B$ $\omega_R = \lambda_B$	Identity $\beta_R = 1$ $\omega_R = 1$
Similarity Criteria				
$\tilde{\Omega}_R = \lambda_A$ $\tau_R = t_R = \frac{\lambda_A}{\lambda_B}$	$\tilde{\Omega}_R = \lambda$ $\tau_R = t_R = 1$	$\tilde{\Omega}_R = \lambda_A$ $\tau_R = t_R = \lambda_A$	$\tilde{\Omega}_R = 1$ $\tau_R = t_R = \frac{1}{\lambda_B}$	$\tilde{\Omega}_R = 1$ $\tau_R = t_R = 1$

The objective of this study was to investigate the possibility of extrapolating accelerated TEDS TTSS charge and discharge tests based on the derived scaling ratios and generated data. The following sections further simplify Equation (32) into known terms and allow for the determination of scaling values. Once the scaling values were obtained, the extrapolated initial conditions, boundary conditions, and extrapolated ideal data points were attainable. To satisfy the study's objective, the TTSS fluid temperature was chosen as the primary parameter for scaling to ensure the precise interpretation of the time-dependent heat storage behavior of the TTSS.

3.8.1. ω-Strain

For this type of coordinate transformation, the scaling ratio for the parameter of interest is restricted to $\lambda_A = 1$. When $\lambda_{A,th} = 1$, the time ratio can be derived as:

$$t_R = \left(\frac{k}{\rho_{th} c_{P,th} T_{th,0}}\right)_R = \left(\frac{\text{energy loss to walls}}{\text{thermocline energy storage}}\right)_R \tag{33}$$

Thus, the time ratio is equivalent to the model and prototype ratio of balance between the energy loss to the walls and energy storage. Other terms in Equation (32) can be similarly simplified using the newly derived time ratio:

$$\begin{aligned}
\lambda_{A,v_{z,in}} &= \left(\frac{k}{\rho_{in} c_{P,in} T_{th,0}}\right)_R, \lambda_{B,v_{z,in}} = \left(\frac{\rho_{th} c_{P,th}}{\rho_{in} c_{P,in}}\right)_R \\
\lambda_{A,T_{in}} &= \left(\frac{c_{P,in} T_{th,0}}{c_{P,th} T_{in,0}}\right)_R, \lambda_{B,T_{in}} = \left(\frac{\rho_{th} c_{P,in} T_{th,0}^2}{k T_{in,0}}\right)_R \\
\lambda_{A,T_{out}} &= \left(\frac{c_{P,out} T_{th,0}}{c_{P,th} T_{out,0}}\right)_R, \lambda_{B,T_{out}} = \left(\frac{\rho_{th} c_{P,out} T_{th,0}^2}{k T_{out,0}}\right)_R \\
\lambda_{A,T_w} &= \left(\frac{1}{T_{w,0}}\right)_R, \lambda_{B,T_w} = \left(\frac{\rho_{th} c_{P,th} T_{th,0}}{k T_{w,0}}\right)_R
\end{aligned} \tag{34}$$

3.8.2. β-Strain

For this type of coordinate transformation, the scaling ratio for the agents of change is restricted to $\lambda_B = 1$. When $\lambda_{B,th} = 1$, then the time ratio can be derived as:

$$t_R = \sqrt{\left(\frac{k}{\rho_{th} c_{P,th} T_{th,0}}\right)_R} = \sqrt{\left(\frac{\text{energy loss to walls}}{\text{thermocline energy storage}}\right)_R} \tag{35}$$

Thus, the time ratio is equivalent to the square root of the model and prototype ratio of balance between the energy loss to the walls and energy storage. Other terms in Equation (32) can be similarly simplified using the newly derived time ratio:

$$
\begin{aligned}
\lambda_{A,v_{z,in}} &= \sqrt{\left(\frac{\rho_{th} c_{P,th} k}{\rho_{in}^2 c_{P,in}^2 T_{th,0}}\right)_R}, \lambda_{B,v_{z,in}} = \left(\frac{\rho_{th} c_{P,th}}{\rho_{in} c_{P,in}}\right)_R \\
\lambda_{A,T_{in}} &= \sqrt{\frac{c_{P,in} k T_{th,0}}{\rho_{th} c_{P,th}^3 T_{in,0}^2}}, \lambda_{B,T_{in}} = \left(\frac{c_{P,in} T_{th,0}}{c_{P,th} T_{in,0}}\right)_R \\
\lambda_{A,T_{out}} &= \sqrt{\frac{c_{P,out} k T_{th,0}}{\rho_{th} c_{P,th}^3 T_{out,0}^2}}, \lambda_{B,T_{out}} = \left(\frac{c_{P,out} T_{th,0}}{c_{P,th} T_{out,0}}\right)_R \\
\lambda_{A,T_w} &= \left(\frac{1}{T_{w,0}}\right)_R, \lambda_{B,T_w} = \sqrt{\left(\frac{\rho_{th} c_{P,th} T_{th,0}}{k T_{w,0}^2}\right)_R}
\end{aligned} \tag{36}
$$

3.8.3. 2–2 Affine

For this type of coordinate transformation, there are no restrictions. The time ratio can be derived as:

$$
t_R = \left(\frac{k}{\rho_{th} c_{P,th} T_{th,0}}\right)_R \frac{1}{\lambda_{A,th}} \tag{37}
$$

The terms in Equation (32) can be similarly simplified using the newly derived time ratio:

$$
\begin{aligned}
\lambda_{A,v_{z,in}} &= \left(\frac{k}{\rho_{in} c_{P,in} T_{th,0}}\right)_R \frac{1}{\lambda_{A,th}}, \lambda_{B,v_{z,in}} = \left(\frac{\rho_{th} c_{P,th}}{\rho_{in} c_{P,in}}\right)_R \\
\lambda_{A,T_{in}} &= \left(\frac{c_{P,in} T_{th,0}}{c_{P,th} T_{in,0}}\right)_R \lambda_{A,th}, \lambda_{B,T_{in}} = \left(\frac{\rho_{th} c_{P,in} T_{th,0}^2}{k T_{in,0}}\right)_R \lambda_{A,th}^2 \\
\lambda_{A,T_{out}} &= \left(\frac{c_{P,out} T_{th,0}}{c_{P,th} T_{out,0}}\right)_R \lambda_{A,th}, \lambda_{B,T_{out}} = \left(\frac{\rho_{th} c_{P,out} T_{th,0}^2}{k T_{out,0}}\right)_R \lambda_{A,th} \\
\lambda_{A,T_w} &= \left(\frac{1}{T_{w,0}}\right)_R, \lambda_{B,T_w} = \left(\frac{\rho_{th} c_{P,th} T_{th,0}}{k T_{w,0}}\right)_R \lambda_{A,th}
\end{aligned} \tag{38}
$$

3.8.4. Others

The other types of coordinate transformation include the dilation and identity methods, which are essentially the same in terms of the time ratio. To fulfill the research objective fo accelerating the heat storage process, scaling types that enforce the time ratio to 1 were incompatible and were excluded from this analysis.

3.9. Nominal Value Selection

To non-dimensionalize the scalable measured values, derived or representative values were selected. Although no derived nominal values were determined, the point of transition between mode 1 (energy charge) and mode 2 (energy discharge) at time 616,036.04 (s) characterized both transients that were exhibited in the TTSS experiments. This was due to both transients including the same data point. Table 2 shows the corresponding values that were attained.

Table 2. Nominal values to non-dimensionalize the generated data. N/A indicates that the value was either not measured or not applicable.

Parameters	Charge Line	TTSS Fluid	TTSS Wall	Discharge Line
Temperature (°C)	166	196	194	187
Specific Heat (kJ/(kg·K))	2.072	2.180	N/A	2.147
Density (kg/m^3)	909	888	N/A	895
k (W/(m·K))	N/A	N/A	15.7	N/A
Velocity (m/s)	0.458	N/A	N/A	0.455

3.10. Scaling Ratio Determination

To demonstrate an accelerated case, the time ratio was set to $t_R = 0.5$ to indicate a charging and discharging process that was twice as fast while conserving the amount of energy that was transferred. Since the nominal value of the TTSS fluid temperature that was selected in Section 3.9 was not derived and was from a point in time, the scaling ratio for the parameter of interest $\lambda_{A_{th}}$ was always 1. According to Equation (9), the scaling ratio for the parameter of interest of the model and the prototype is about normalized values. When the nominal value is a point in time, the corresponding normalized values are always equivalent when they are ideally scaled. Thus, the ω-strain scaling was the only valid option for this study, given the previous scaling decisions (2–2 affine would have been applicable but would revert back to ω-strain when $\lambda_{A_{th}} = 1$). For this type of scaling, the time derivative scaling ratio is $\lambda_{B_{th}} = \lambda_{A_{th}}/t_R = 2$.

To determine the accelerated case, the TTSS fluid temperatures and properties that provided $\lambda_{B_{th}} = 2$ were explored. Due to the temperature-dependent material property restrictions, only one set of fluid properties yielded a result that was close to the goal value and calculated a new time ratio of 0.502. Based on the TTSS fluid temperature of the accelerated case, Table 3 shows the associated nominal values.

Table 3. Accelerated nominal values used to non-dimensionalize the extrapolated data. N/A indicates that the value was either not measured or not applicable.

Parameters	Charge Line	TTSS Fluid	TTSS Wall	Discharge Line
Temperature (°C)	354	418	399	414
Specific Heat (J/(kg·K))	2.781	3.037	N/A	2.959
Density (kg/m^3)	763	708	N/A	725
k (W/(m·K))	N/A	N/A	18.9	N/A
Velocity (m/s)	0.458	N/A	N/A	0.455

To calculate the other scaling ratios that were derived for the ω-strain case based on the TTSS fluid temperature scaling, we solved Equation (34) while satisfying the time ratio of 0.503. The obtained values are provided in Table 4.

Table 4. Scaling ratio values used to attain a doubly accelerated energy charge and discharge process.

Parameters	λ_A	λ_B
T_{th}	1.000	1.993
T_{in}	1.037	2.068
T_{out}	1.027	2.046
T_w	0.4692	0.9351
$v_{z,in}$	0.5086	1.014

Although, β-strain scaling was not applicable, calculations that achieved a time ratio of 0.5 were also examined. The outcome indicated that the time ratio 0.5 could not be produced with the current assumptions applied. The smallest possible time ratio was 0.622.

4. Results and Discussion

The TEDS facility conducted tests to observe the charging and discharging modes for a thermocline storage system in TEDS. The thermocline was charged until the system reached the desired target temperature. It then switched to discharging mode to remove excess heat. The temperature and velocity data were analyzed to determine the β, ω, $\dot{\omega}$, and D parameters and the temperature and velocity data were then normalized with the nominal values that are listed in Table 3.

4.1. Thermocline Centerline Results

The temperature data were analyzed in locations that were representative of the thermocline inlet, outlet, and centerline positions. The data were smoothed using a Savitzky–Golay filter to reduce noise. Figure 3 shows the normalized centerline thermocline temperature trace for the duration of the test, with both operation modes listed as well.

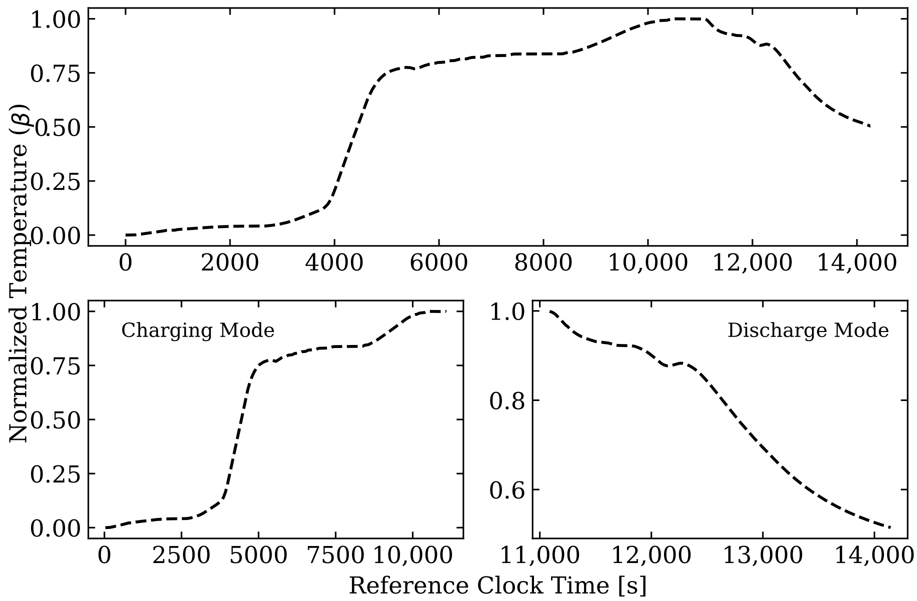

Figure 3. Normalized temperature data from the thermocline centerline location: reference value, T_o = 418 °C.

The ω-strain analysis was performed on both operation modes using the λ_A and λ_B values for each location, as specified in Table 4. Because local equilibrium points create singularities in DSS, each mode was separated into separate regions of interest to avoid this issue.

4.1.1. Charging Mode

The centerline charging mode analysis was separated into two phases due to the presence of a local equilibrium position that was reached in charging mode between roughly 5000 (s) < t < 8000 (s), as seen in Figure 3. Figures 4 and 5 show the β (normalized raw data), ω (first derivative of β), $\dot{\omega}$ (first derivative of ω or second derivative of β), and D (second-order term, also known as the temporal displacement rate) values for the original measured data and the scaled data from using the $\lambda_A = 1.000$ and $\lambda_B = 1.993$ values, which corresponded to a process time ratio of $\tau_R = 0.502$. The accelerated data occurred in roughly half the time of the original charging sequence. For a simpler visualization of this, the reference time is presented as the relative reference time passed.

Figures 4 and 5 represent the first and second phases of the charging mode, based on the singularity. Each projected point was 0.502 of the past data time, but at different magnitudes that were not consistent with the time ratio. This was due to the scaling ratios derived in Section 3.8, in which the scaling was non-linear to the time ratio and was fluid property-dependent. An important aspect of using the ω-strain scaling is that the scaled and original datasets need to have equivalent temporal displacement rates. When the X-axis was given as fractions of the maximum time, it could be seen that this requirement was achieved and that the two processes were invariant. Additionally, the scaled process curves for both phases in Figure 6 show that there was an overlap between the curves, indicating that the ω-strain scaling was successfully applied to the data and that there was no distortion within the thermocline temperature data. This represented the required temperature increase and the first- and second-order effects that were needed to maintain no distortion and allow the thermocline to be charged twice as a fast in this specific test. If the TEDS facility were to design a future experiment for half-time but desired the same amount of stored energy, it is expected that the generated data would follow the accelerated data by using the given boundary conditions at the times derived by DSS. This projection of data would support the signal conversion for incoming and outgoing information for DETAIL.

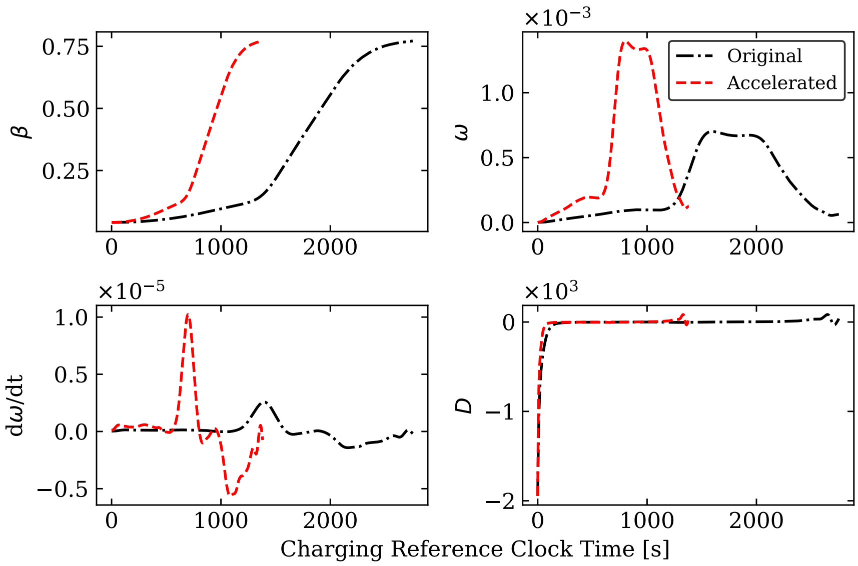

Figure 4. Scaling comparison of charging mode at the centerline, phase 1.

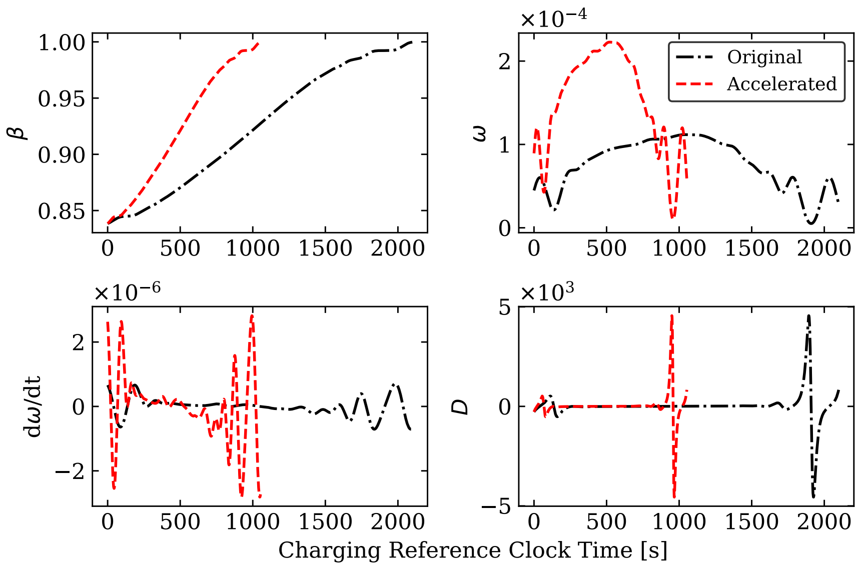

Figure 5. Scaling comparison of charging mode at the centerline, phase 2.

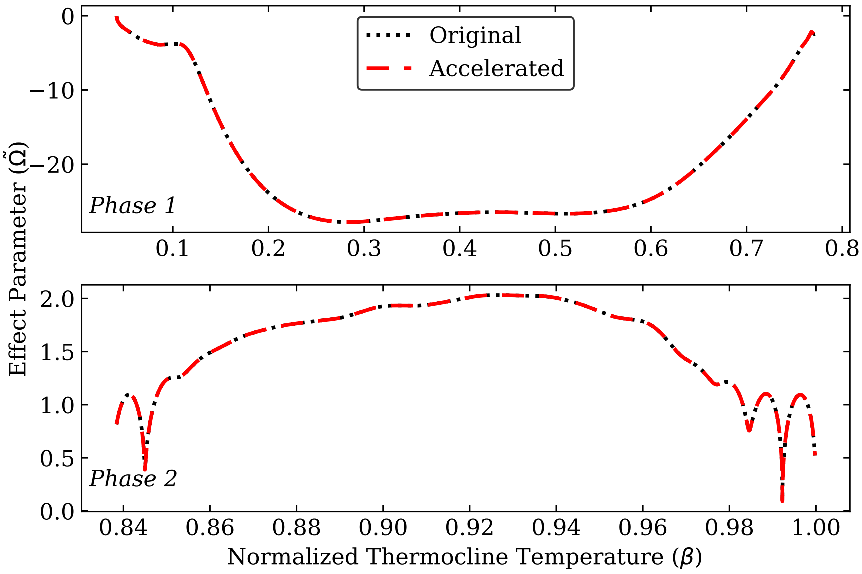

Figure 6. Scaled process curves of charging mode at the centerline.

4.1.2. Discharging Mode

The thermocline discharge data were similarly analyzed using the same λ_A, λ_B, and τ_R values from Section 4.1.1 to construct the accelerated dataset. Similar to the charging mode, a period of equilibrium was reached between the reference time of 11,500 (s) < t < 12,000 (s), which required the discharge data to be split into two analysis phases.

Figures 7 and 8 show the main DSS parameters for each phase in discharging mode. The magnitude agreement between the temporal displacement rates were maintained and the transient features of both the ω and $\dot{\omega}$ parameters were seen to be magnified in the accelerated case. The temporal displacement rate changed sign twice during the first phase, indicating that the discharge process switched from a dilated process time interval to a contracted process time interval and then back to dilated. In other words, the relative change between the reference time and process time shifted in magnitude, which displayed the complexity of the data geometry.

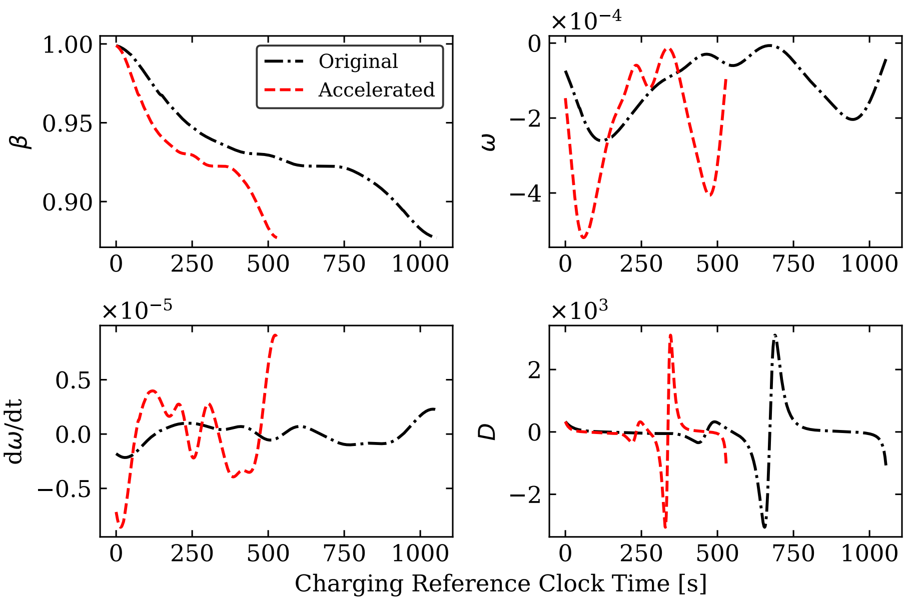

Figure 7. Scaling comparison of discharging mode at the centerline, phase 1.

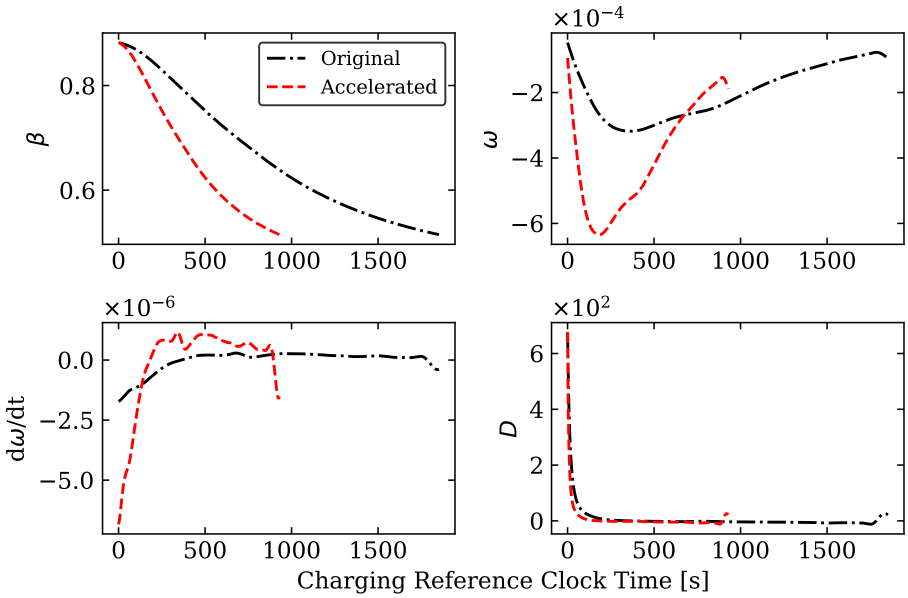

Figure 8. Scaling comparison of discharging mode at the centerline, phase 2.

Figures 7 and 8 represent the first and second phases of discharging mode, based on the singularity. As shown for charging mode in Figures 4 and 5, each accelerated data point was 0.502 of the original data time at different magnitudes due to the non-linear scaling ratio derivation (see Section 3.8). Figure 9 shows the scaled process curves for both phases in discharging mode. Because the ω-strain scaling was applied to each DSS parameter and the temporal displacement rates were invariant, the scaled process curve separation was close to zero. This indicated that the accelerated discharge case had little to no scaling distortion and, similarly to charging mode, if derived boundary conditions were to be used in TEDS, the double acceleration would follow the projected data.

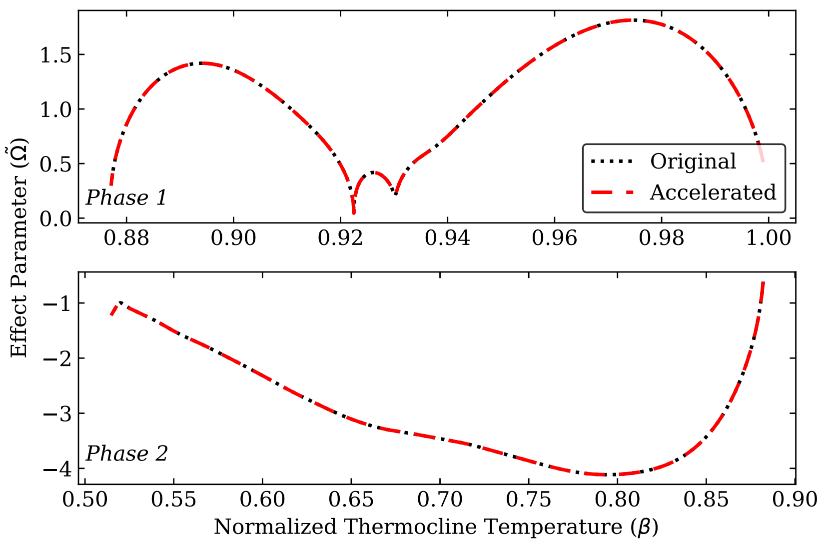

Figure 9. Scaled process curves of discharging mode at the centerline.

4.2. Thermocline Inlet Results

The normalized inlet temperature traces are shown in Figure 10, with data separated for the charging and discharging modes provided as well. For the inlet location, the $\lambda_A = 1.037$, $\lambda_B = 2.068$, and resulting $\tau_R = 0.501$ values were not identical to the thermocline centerline λ values, as discussed in Table 4. The change in temperature trends was attributed to the flow direction at different modes. In charging mode, the hot fluid flowed from the thermocline inlet and out of the thermocline outlet. On the other hand, discharging mode injected cold fluid (relatively low temperature compared to the hot fluid temperature) in the thermocline outlet that was then ejected out of the thermocline inlet, thus reversing the flow. This explained the delayed temperature response compared to the thermocline temperatures in Figure 3, as the interface of the cold and hot fluid traveled back to the inlet location.

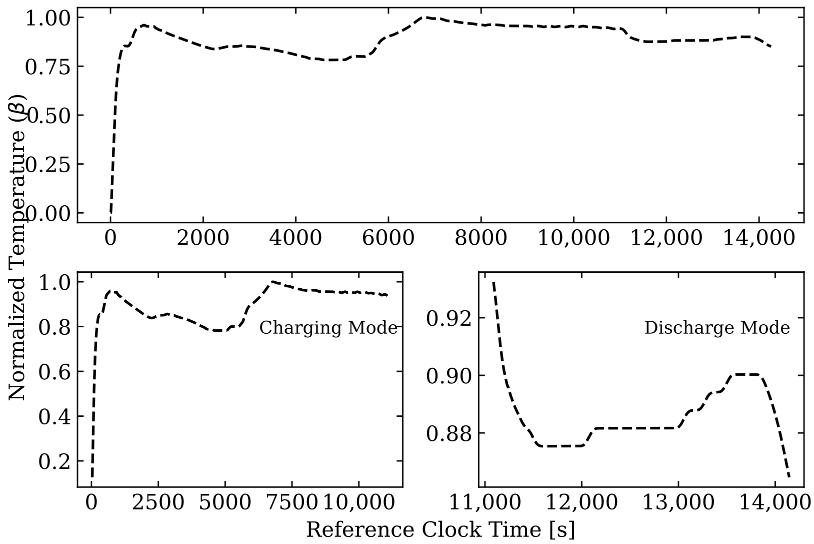

Figure 10. Normalized temperature data from the thermocline inlet location: reference value, T_o = 354 °C.

4.2.1. Charging Mode

The charging mode data for the inlet location needed to be separated into two phases, similar to the previous sections. As expected, the charging data saw a temperature plateau region that was similar to that observed in the thermocline centerline data. The DSS parameters for both phases are plotted in Figures 11 and 12, in which it can be seen that the temporal displacement rates were equivalent once again. However, because the λ_A value was not exactly 1.0, the beta traces were slightly offset in magnitude. This offset was most observable in the second phase, for which it was analyzed over a short time interval.

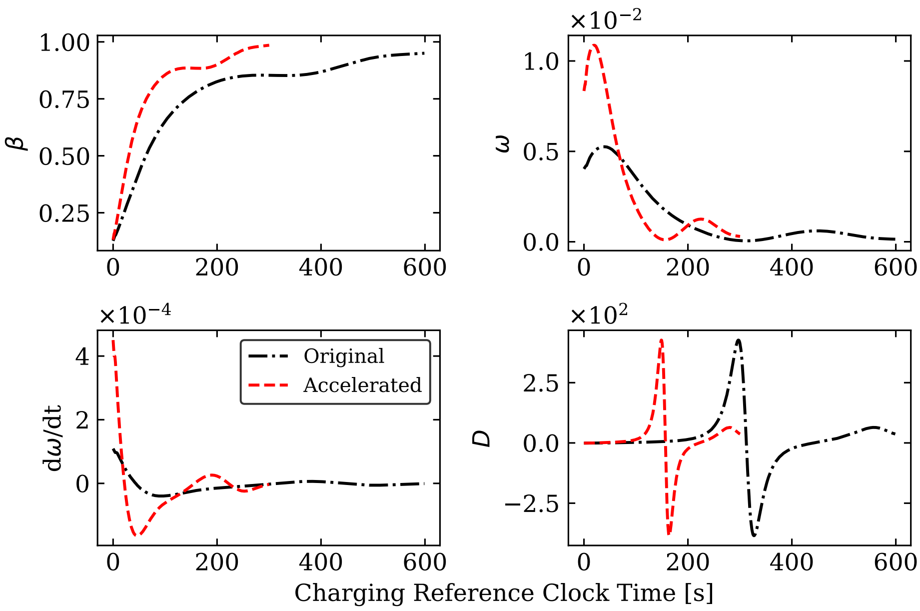

Figure 11. Comparison of charging mode at the inlet location, phase 1.

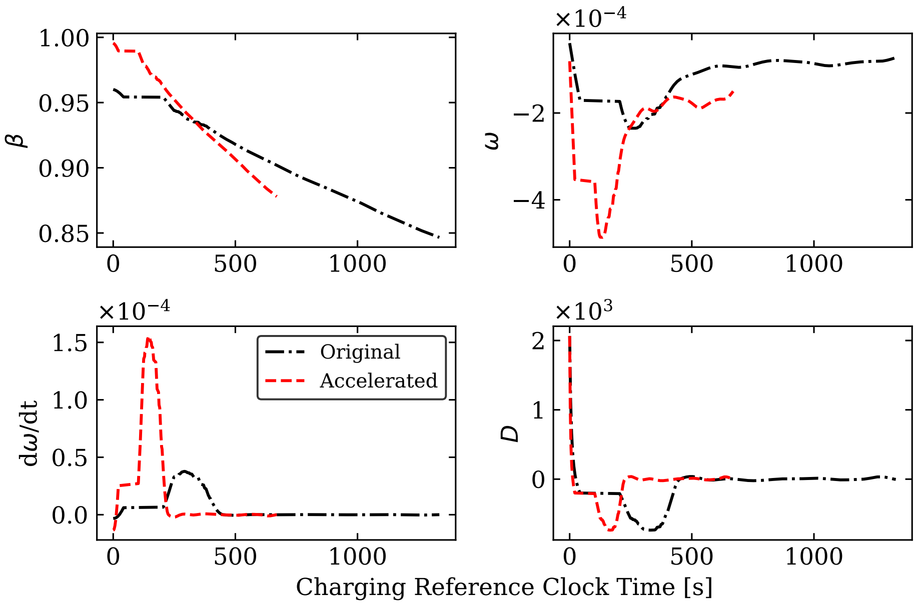

Figure 12. Comparison of charging mode at the inlet location, phase 2.

The comparison of the scaled process curves in Figure 13 shows that curve separation occurred in both phases. This was expected because the λ_A value was not exactly 1.0 and the shift of the curve was more prominent in the second phase, primarily due to the short time interval that was used for the analysis, which emphasized the separation more. In the first phase, the separation became more pronounced as the charging phase evolved. This showed that slight deviations from the ω-strain requirement of $\lambda_A = 1$ could result in a process being scaled more by 2–2 affine scaling. However, the matched $\tilde{\Omega}$ magnitudes indicated that the transient aspect of the process time was preserved between the two cases. If the effect parameter values and normalized thermocline temperatures were to be divided by their corresponding scaling ratios of $\lambda_A = 1.037$, the data points would overlap perfectly, which is an indication of perfect similitude.

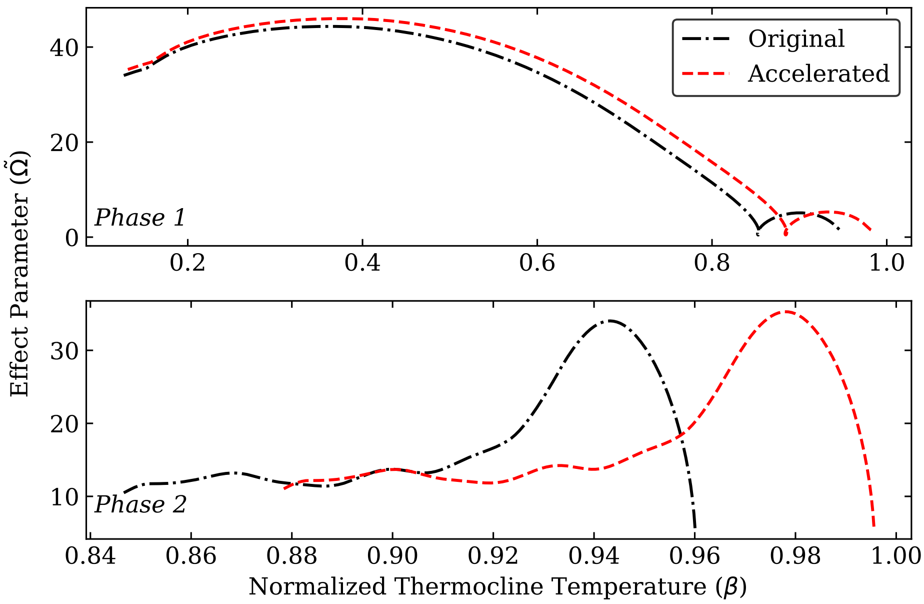

Figure 13. Scaled process curves of charging mode at the inlet location.

4.2.2. Discharging Mode

The DSS parameters for the thermocline inlet location are shown in Figures 14 and 15. Similarly, trends were observed in the matched temporal displacement rates, indicating that the process time intervals were matched between the original and scaled accelerated scenarios. Additionally, the features of the ω and $\dot{\omega}$ terms were magnified by the accelerated case, as expected. The shift in β values appeared to be magnified due to the short time interval that was considered for the discharge phasing and the axis limits.

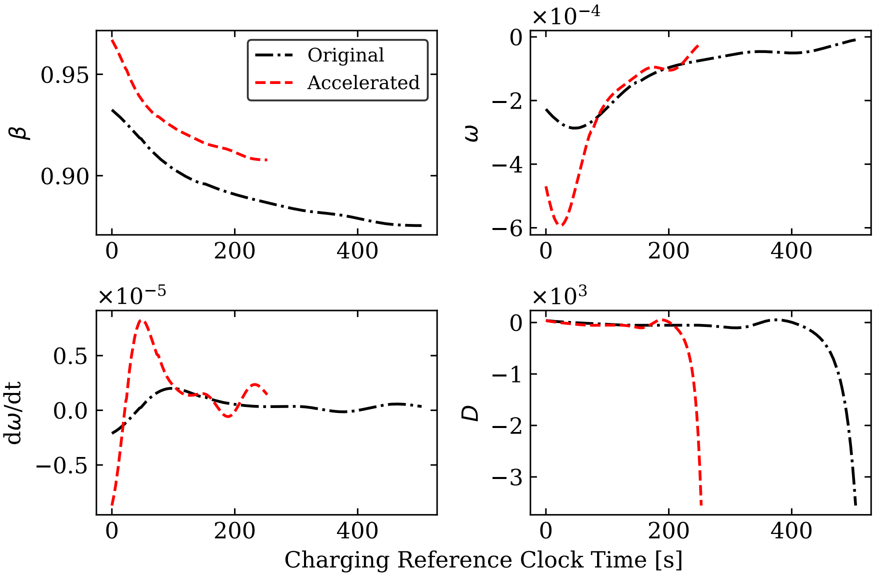

Figure 14. Comparison of discharging mode at the inlet location, phase 1.

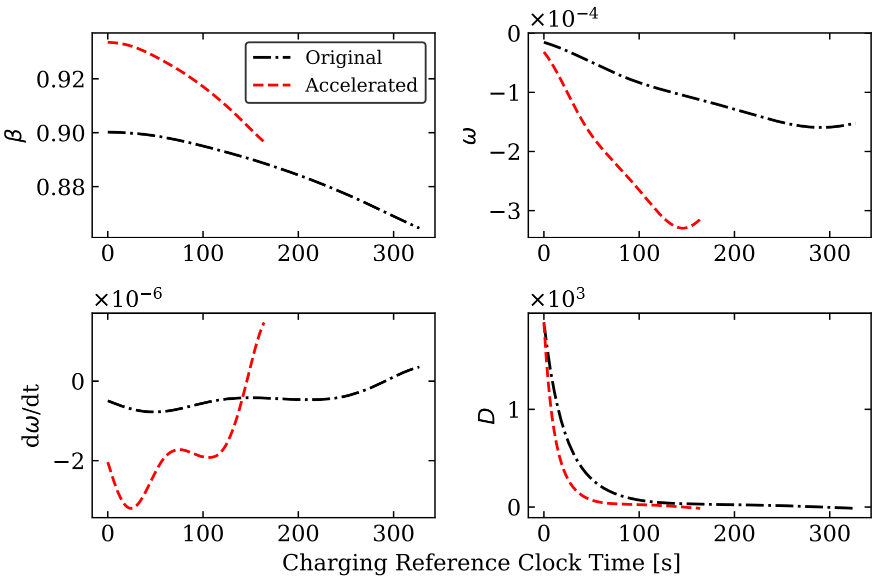

Figure 15. Comparison of discharging mode at the inlet location, phase 2.

The curve separation that can be seen in Figure 16 was expected due to the slight deviation in λ_A not being exactly equal to 1. As noted in the charging section, this separation appeared to be magnified due to the small axis limits that were covered by the discharging mode, for which data did not occur in a local equilibrium position. In Figure 10, it can be seen that there were several periods of temperature plateau, which limited the data regions that were available for the DSS analysis. As mentioned for charging mode, the observed separations were the result of scaling and, if they were to be divided by the scaling ratio, this would in fact overlap.

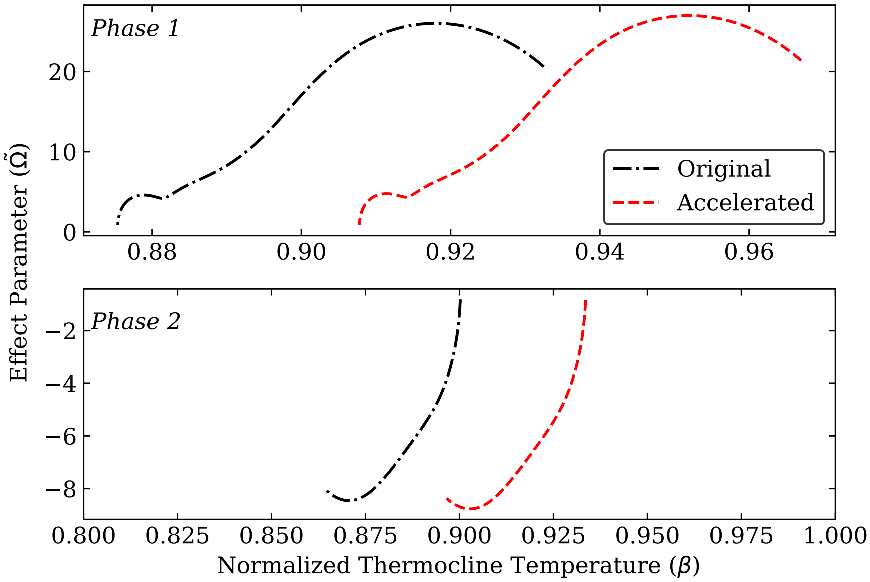

Figure 16. Scaled process curves of discharging mode at the inlet location.

4.3. Thermocline Outlet Results

The normalized thermocline outlet temperature data and reference values that were used for the normalization are shown in Figure 17, along with the separated data that were considered in the charging and discharging mode analysis. Compared to the inlet location, the charging data had a similar temperature plateau region, which also required the charging data to be analyzed in two phases. However, the discharging mode data recorded a substantially smoother temperature decrease without the plateau regions that were seen in the two other locations. This resulted in the discharging mode data being analyzed in one dataset. Due to the flow reversal during mode transitions, the timing of the trend changes was quicker than that of the thermocline centerline and inlet temperatures.

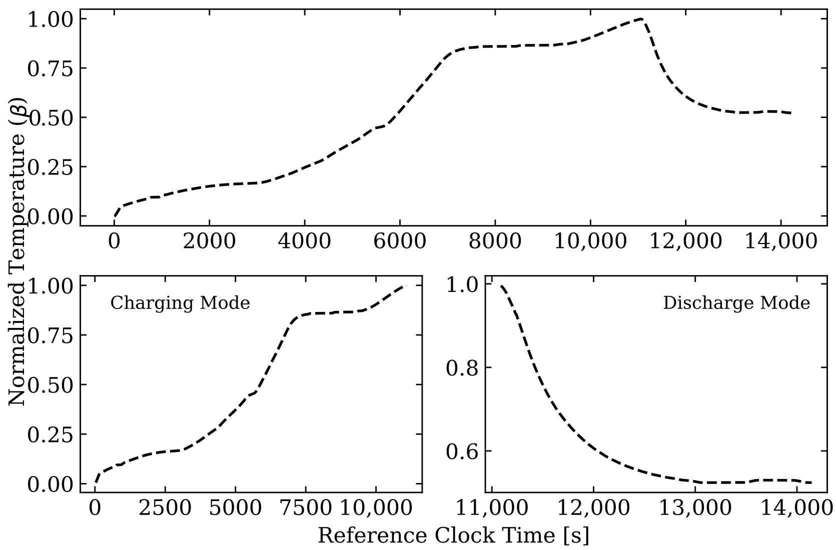

Figure 17. Normalized temperature data from the thermocline outlet location: reference value, T_o = 414 °C.

4.3.1. Charging Mode

The β values presented in Figures 18 and 19 show that the 2–2 affine scaling for the outlet location ($\lambda_A = 1.027$) required the scaled dataset to a have a slightly higher normalized outlet temperature than that of the original test. However, because the temporal displacement was preserved, the transient process time similitude was maintained. Since the scaling ratio was different from that at the thermocline inlet ($\lambda_{A,inltet} = 1.037 > \lambda_{A,outlet} = 1.027$), the displacements that are shown in Figures 18 and 19 and Figures 11 and 12 were not equivalent. Again, these differences in scaling ratios were a product of the DSS derivations, based on physics relationships and fluid properties. If other constraints were to exist, the difference would potentially be larger but would not affect the accuracy of the projection.

The scaled process curve of the first phase (shown in Figure 20) shows that there was very minimal separation between the two datasets. The separation distance became more pronounced as the outlet temperature increased toward its maximum value for the first phase. The separation was more pronounced in the second phase, primarily due to the small axis limits for the figure, and the differences of 2.07% became more apparent at higher β values. As noted in the inlet case, the accelerated case required the normalized temperature to be slightly larger than that of the original case. It should be noted that the separation was not a result of the derivation but was recognized as the necessary change in the phase space ($\tilde{\Omega} - \beta$) to guarantee the perfect overlap of the thermocline temperatures.

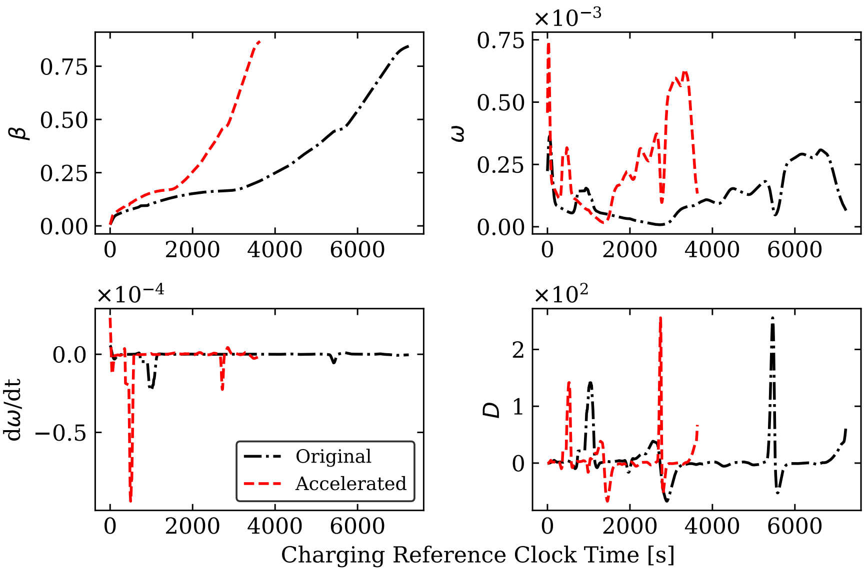

Figure 18. Comparison of charging mode at the outlet location, phase 1.

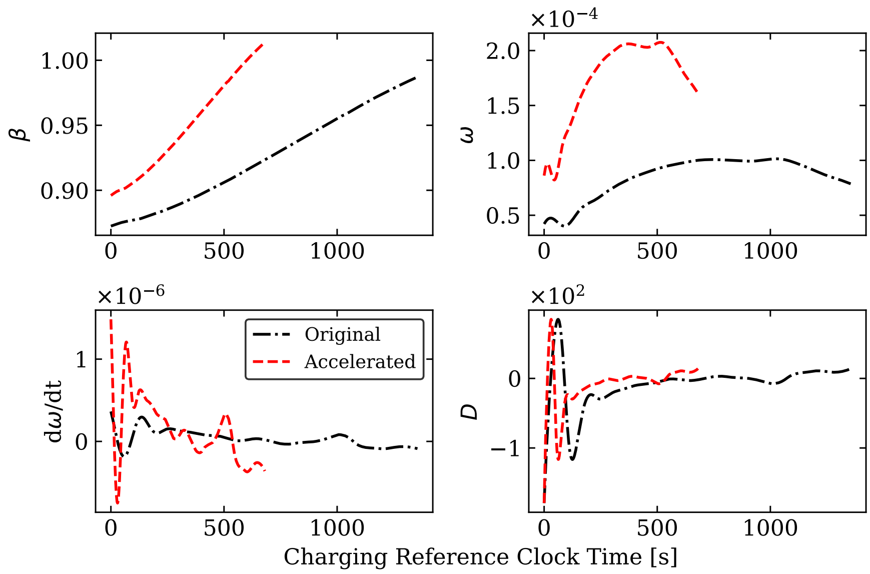

Figure 19. Comparison of charging mode at the outlet location, phase 2.

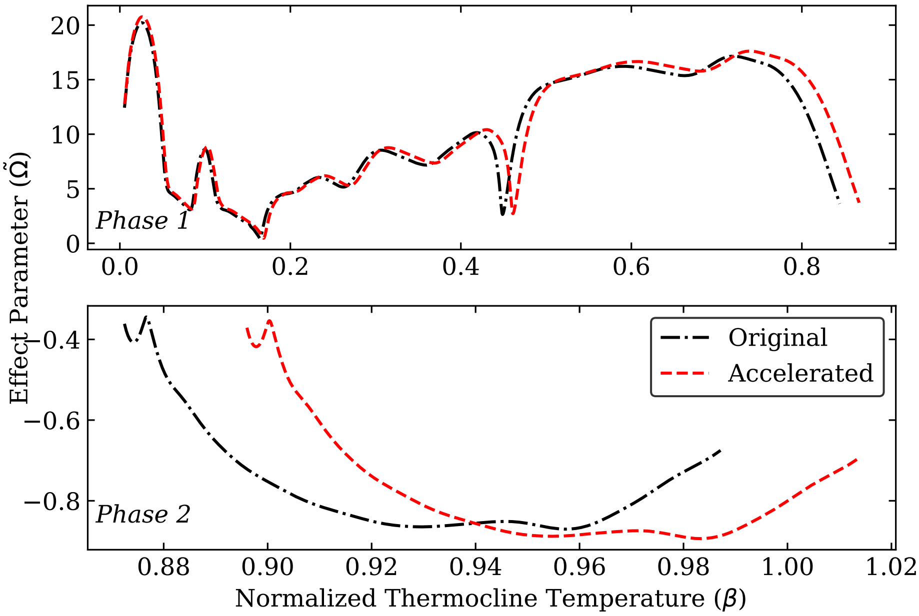

Figure 20. Scaled process curves of charging mode at the outlet location.

4.3.2. Discharging Mode

The DSS parameters for the thermocline outlet location are plotted in Figure 21, which did not experience the temperature plateau regions that were observed in the inlet location data. As with the other results, it was observed that the temporal displacement rate was preserved in the accelerated case, as required for the scaling type. The accelerated $\dot{\omega}$ had to be larger than the original data by a scale factor of λ_B^2/λ_A, which resulted from substituting Equations (9) and (10) into the definition of $\dot{\omega}$. Since the time ratio ($t_R = \lambda_A/\lambda_B$) was equivalent for all parameters and locations, the timing was always roughly half of that of the original data. It was the determination of the magnitude of each temporal data point that produced the DSS data projection value.

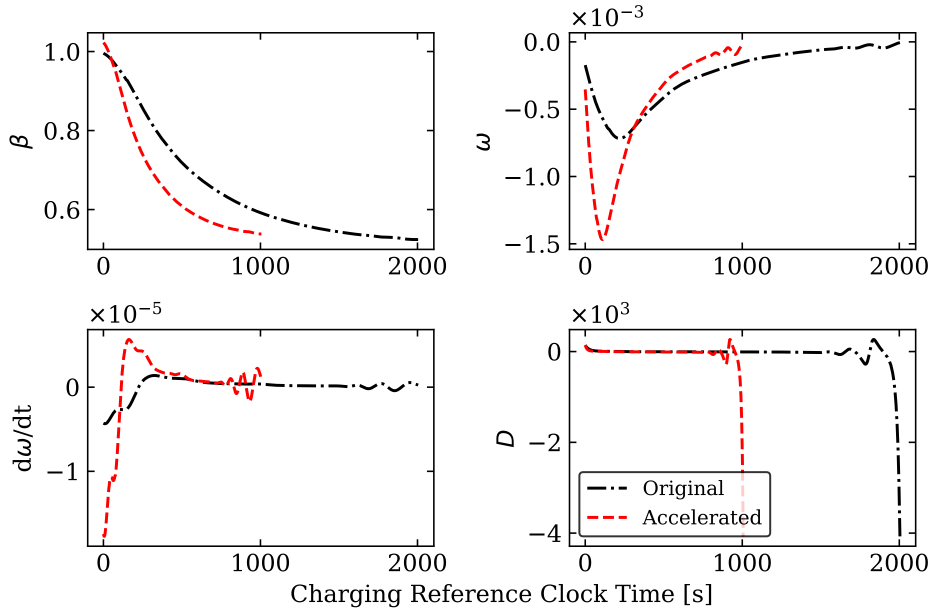

Figure 21. Comparison of discharging mode at the outlet location.

The comparison of the scaled process curves presented in Figure 22 shows that the magnitudes of the normalized temperature rates of change ($\tilde{\Omega}$) were maintained across discharging mode. This indicated that the process action and ω term were correctly scaled to preserve the process similitude. A similar β shift was seen for the accelerated data because of $\lambda_A = 1.027$, with the separation becoming more pronounced at higher β values, which was at the beginning of the operation mode.

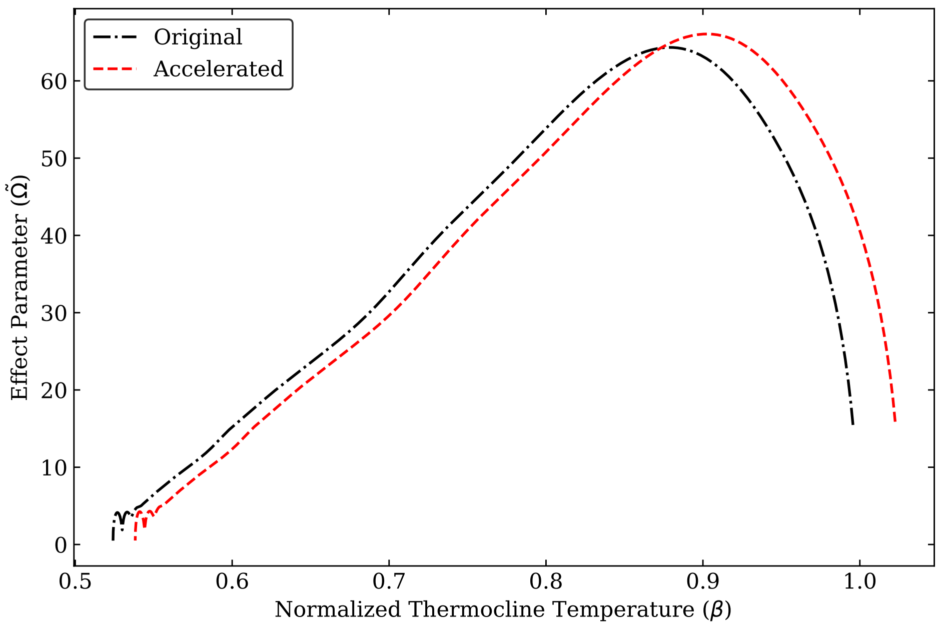

Figure 22. Scaled process curves of discharging mode at the outlet location.

4.4. Velocity Results

The velocity data were determined from two inline flowmeters located on the outlet side of the thermocline system. Each operation mode (charging/discharging) has a dedicated flow path that branches out from the system's main outlet piping. Because of the flow paths and the operation control configuration of the thermocline system, when one operation mode is active, there is no fluid flow through the flow path of the other operation mode. Due to the high noise and oscillating values for the velocity that were determined from the flowmeter FM-202 for the charging mode, an analysis was not performed on the charging mode velocity. A limitation of DSS is the difficulty in analyzing the oscillating data. While some data reach natural equilibrium when a process undergoes a shift in behavior (such as reaching a peak temperature), oscillating data primarily indicate that the instrument is having difficulty collecting a smooth signal. The $\lambda_A = 0.5086$ and $\lambda_B = 1.014$ values that were used to scale the data were taken from Table 4 and applied to discharging mode. In contrast to the inlet and outlet locations, the velocity scaling ratio was significantly lower than the thermocline centerline temperature. This was due to the inverse proportional relationship of the energy-governing equation against the proportional relationships of the inlet and outlet temperatures:

$$\lambda_{B,T} \approx \lambda_{A,v_z} \lambda_{A,T} \approx \frac{\lambda_{A,inlet,outlet}}{\lambda_{A,T}} \tag{39}$$

If the system acceleration were set to more than double, the velocity scaling ratio would potentially drop to lower values.

Discharging Mode

The discharging mode data were analyzed from flowmeter FM-201 and the normalized flow velocity is plotted in Figure 23. Because several local velocity equilibrium points were reached in discharging mode, four separate phases were analyzed within the dataset to complete the DSS analysis.

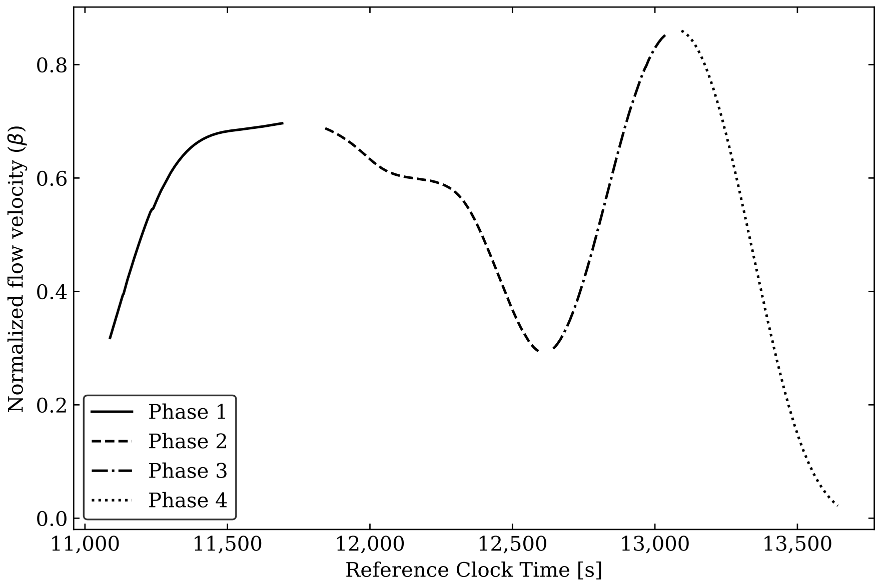

Figure 23. Normalized flow velocity data from discharging mode.

Figure 24 shows the scaled process curves for all four phases of discharging mode, in which several features can be observed. First, both the β and $\tilde{\Omega}$ accelerated values shifted from the original data. The β values were roughly halved, based on the $\lambda_A \approx 0.5$ parameter. Because the λ_B value was close to 1, the flow velocity was scaled by the β-strain scaling type, as described in Table 1. This resulted in a shift toward the $\tilde{\Omega}$ values by a factor of λ_A. Regardless of the observed shifts in data, the data geometry remained identical, which was evidence of the conserved physics. This highlighted that preserving the process similitude in the temperature response corresponded to projections being further away, which resembled a different scaling mode for the flow velocity. This result suggested that scaled systems are able to perfectly preserve every parameter response without the introduction of scaling distortion, as long as the governing equations capture the true agents of change. If any dominating agent of change were missing, the determined projection would potentially be invalid. However, this is not a weakness of the DSS methodology but rather a strength, since the detection of missing physics is helpful in the theoretical modeling of observed phenomena.

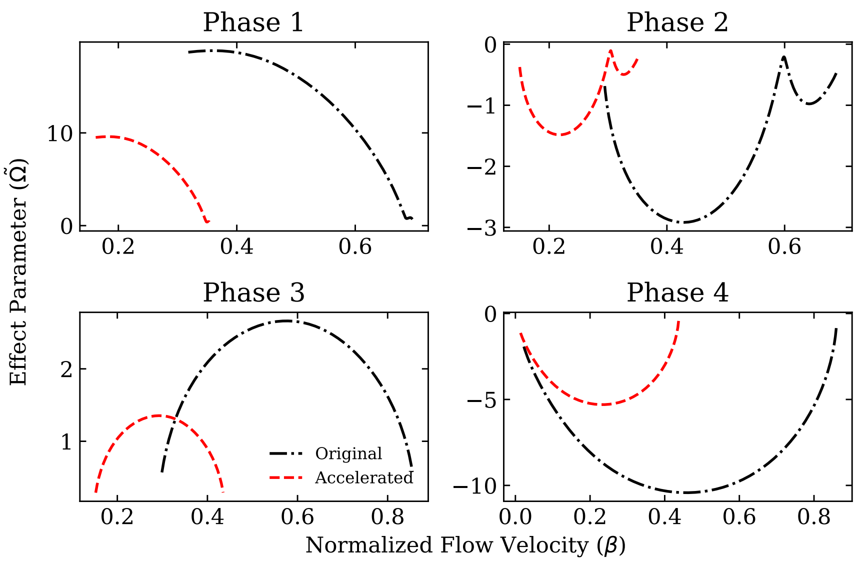

Figure 24. Scaled process curves of the flow velocity in discharging mode.

4.5. Overall

Figures 3–24 all represent the doubly accelerated case, based on experimental charging and discharging data. When the X-axis was the reference time, the timing of each corresponding variable shifted to exactly 0.502 times the original time. This in itself was not particularly significant since "half of the time interval" can be imagined without difficulty. If this were a simulation model or experiment that were designed based on the DSS analysis, then the fact that transients occur at half of the original time would be remarkable. However, this was outside of the scope of our objective of "projecting experimental conditions", without running additional experiments.

The outstanding findings from Figures 3–24 include the determined scaled magnitudes of each time-dependent point for charging mode, discharging mode, and TTSS temperatures. Every point was projected while conserving the physics and achieved the same amount of energy charge and discharge. The values that were set for each parameter to accomplish a doubly accelerated system, such as thermocline porosity, inlet velocity, pressure, ambient temperature, heater power and pressure, and projected maximum temperature for charge line, discharge line, and wall temperatures, provided information that could define the experimental initial and boundary conditions to achieve representative and conserved results that avoided the use of a design defined by the Edisonian approach or solely relying on engineering intuition. Figures 3–24 represent the large potential for designing reliable experiments that are defined by engineering limits and research objectives.

5. Conclusions

The TTSS of TEDS was selected to represent a case of data extrapolation to design facility tests based on the generated data. Based on flow conditions, geometry, materials, and transient behavior, the fundamental equations were determined and discretized to include TTSS inlet and outlet parameters. The equations were non-dimensionalized according to the DSS definition and scaled formats were derived for the relevant phase space coordination transformation methods introduced in Table 1. To accelerate the given TTSS data, static time-scaling methods, such as dilation and identity, were excluded from the analysis. By setting the TTSS centerline mid-axial temperature as the property to preserve, the phase space scaling was further restricted to the ω-strain method (i.e., the normalized temperature scaling ratio was $\lambda_A = 1$) to maintain identical relative TTSS temperature magnitudes when normalizing with the temperature recorded during the transition between charging and discharging transients. To be capable of $\lambda_A \neq 1$, the value used to normalize the TTSS temperature would either have to be derived or be a constant that is shared between the original and accelerated test cases. When attempting to make λ_A equivalent to the time ratio (β-strain scaling method), it was concluded that the goal time ratio could not be achieved due to the balance of the therminol fluid density, therminol fluid specific heat, and stainless steel wall conductive heat transfer coefficient when the TTSS fluid temperature was altered.

After setting the global time ratio to 0.5 (twice as fast) and following the ω-strain scaling, the scaling ratios for the TTSS inlet, outlet, and wall parameters were calculated and are shown in Table 4. As anticipated, the derived twice-accelerated case showed perfect scaling for the TTSS temperature $\beta - \tilde{\Omega}$ distributions (overlapping of data is proof of ideal scaling) and demonstrated the data drift in comparison to the original dataset using $\beta-$time representation. On the other hand, the other scaled parameters showed shifts toward the $\beta - \tilde{\Omega}$ distribution as well; however, when dividing the scaling ratios into the corresponding parameters, the accelerated data overlapped to indicate perfect scaling. The data extrapolation was successful and provided a TTSS test that achieved the same energy charge and discharge in half the time.

While abiding by scaling restrictions, such as unchanged geometry and materials, the accelerated test was calculated by extrapolating the original dataset using the DSS methodology. One of the unexpected yet significant findings of this scaling activity was that without the freedom to change the geometry of the system, the scaling ratios were about system properties (e.g., fluid density). The distribution of these properties varied from one to another and restricted the range of feasible scaling ratio values. For future reference, if more dramatic test acceleration were to be desired without varying geometry, a change in the fluid medium of the TTSS would have to be considered.

Author Contributions: Conceptualization, R.Y. and A.D.; methodology, R.Y.; data curation and data analysis, A.D.; supervision, A.E.; resources, A.E.; writing—original draft preparation, R.Y., A.D. and A.E.; writing—review and editing, A.E.; project administration, A.E.; funding acquisition, A.E. All authors have read and agreed to the published version of the manuscript.

Funding: This manuscript was funded by Battelle Energy Alliance, LLC under contract number DE-AC07-05ID14517 with the US Department of Energy. The United States Government retains and the publisher, by accepting the article for publication, acknowledges that the US Government retains a non-exclusive, paid-up, irrevocable, worldwide license to publish or reproduce the published form of this manuscript, or allow others to do so, for US Government purposes.

Institutional Review Board Statement: This document was reviewed under the Peer Review System and Lab Review System of INL to ensure the quality of this document and verification of disclosable data under data classification regulations.

Informed Consent Statement: Not applicable.

Data Availability Statement: The data are available within this document. Normalized values and other parameters are provided and are capable of calculating the original dataset.

Acknowledgments: The authors would like to thank the INL IES program for providing the funding for the application of DSS to TEDS and Terry Morton, part of the TEDS facility, for providing facility reports and data to make this study possible.

Conflicts of Interest: The authors declare no conflict of interest. The funders had no role in the design of the study; in the collection, analyses, or interpretation of data; in the writing of the manuscript, or in the decision to publish the results.

Abbreviations

The following abbreviations are used in this manuscript:

CMT	Core Makeup Tank
DETAIL	Dynamic Energy Transport and Integration Laboratory
DSS	Dynamical System Scaling
INL	Idaho National Laboratory
IES	Integrated Energy System
NPP	Nuclear Power Plant
TEDS	Thermal Energy Distribution System
TTSS	Thermocline Thermal Storage System

References

1. Morton, T.J. Integrated Energy Systems Experimental Systems Development. United States Department of Energy. 2020. Available online: https://www.osti.gov/servlets/purl/1668842 (accessed on 10 March 2022).
2. Al-Ghussain, L.; Abubaker, A.M.; Darwish Ahmad, A. Superposition of Renewable-Energy Supply from Multiple Sites Maximizes Demand-Matching: Towards 100% Renewable Grids in 2050. *Appl. Energy* **2021**, *284*, 116402. [CrossRef]
3. Levin, T.; Botterud, A.; Mann, W.N.; Kwon, J.; Zhou, Z. Extreme Weather and Electricity Markets: Key Lessons from the February 2021 Texas Crisis. *Joule* **2022**, *6*, 1–7. [CrossRef]
4. Eliana, R. Argentina Capital Hit by Major Power Outage Amid Heat Wave. News Article: Reuters. 11 January 2022. Available online: https://www.reuters.com/world/americas/argentina-capital-hit-by-major-power-outage-amid-heat-wave-2022-01-11/ (accessed on 31 May 2022).
5. Asgary, A.; Mousavi-Jahromi, Y. Power Outage, Business Continuity and Businesses' Choices of Power Outage Mitigation Measures. *Am. J. Econ. Bus. Adm.* **2011**, *3*, 312–320. [CrossRef]
6. Bragg-Sitton, S.M. Next Generation Nuclear Energy: Advanced Reactors and Integrated Energy Systems. United States. 2022. Available online: https://www.osti.gov/servlets/purl/1865609 (accessed on 31 May 2022).
7. Marting, R.P.; Frepoli, C. *Design-Basis Accident Analysis Methods for Light-Water Nuclear Power Plants*, 1st ed.; World Scientific: Singapore, 2019; pp. 181–263. [CrossRef]

8. Yoshiura, R.; Epiney, A.; Mohammad, A. Integration of Dynamical System Scaling to RAVEN and Facility Application. INL EXT-21-64507-Rev000, Idaho National Laboratory. 2021. Available online: https://www.osti.gov/biblio/1822257/ (accessed on 10 March 2022).
9. Yoshiura, R.K. Dynamic System Scaling Application to Accelerated Nuclear Fuel Testing. In Proceedings of the 19th International Topical Meeting on Nuclear Thermal Hydraulics, Brussels, Belgium, 6–11 March 2022.
10. Sabharwall, P.; O'Brien, J.E.; McKellar, M.G.; Housley, G.K.; Bragg-Sitton, S.M.; Boardman, R.D. *Scaling Analysis Techniques to Establish Experimental Infrastructure for Component, Subsystem, and Integrated System Testing*; INL/EXT-15-34456; Idaho National Laboratory: Idaho Falls, ID, USA, 2015. [CrossRef]
11. Frick, K.; Bragg-Sitton, S.; Rabiti, C. Modeling the Idaho National Laboratory Thermal-Energy Distribution System (TEDS) in the Modelica Ecosystem. *Energies* **2020**, *13*, 6353. [CrossRef]
12. Stoots, C.; Duenas, D.M.; Sabharwall, P.; O'Brien, J.E.; Soo Yoo, J.; Bragg-Sitton, S. *Thermal Energy Delivery System Design Basis Report*; INL/EXT-18-51351-Rev000; Idaho National Laboratory: Idaho Falls, ID, USA, 2018. [CrossRef]
13. Frick, K.; Bragg-Sitton, S.; Garrouste, M. *Validation and Verification Methodology for INL Modelica-Based TEDS Models via Experimental Results*; INL EXT-21-64408-Rev000; Idaho National Laboratory: Idaho Falls, ID, USA, 2021. [CrossRef]
14. Reyes, J.N. The Dynamical System Scaling Methodology. In Proceedings of the 16th International Topical Meeting on Nuclear Thermal Hydraulics, Chicago, IL, USA, 30 August–4 September 2015.
15. Reyes, J.N.; Frepoli, C.; Yurko, J.P. The Dynamical System Scaling Methodology: Comparing Dimensionless Governing Equations with the H2TS and FSA Methodologies. In Proceedings of the 16th International Topical Meeting on Nuclear Thermal Hydraulics, Chicago, IL, USA, 30 August–4 September 2015.
16. Einstein, A.; Infeld, L. *The Evolution of Physics from Early Concepts to Relativity and Quanta*, 1st ed.; Simon and Schuster Publisher: New York, NY, USA, 1966. [CrossRef]
17. Gunn, D.J. Transfer of heat or mass to particles in fixed and fluidised beds. *Int. J. Heat Transf.* **1978**, *21*, 467. [CrossRef]
18. Esence, T.; Brunch, A.; Molina, S.; Stutz, B.; Fourmigue, J.F. A review on experience feedback and numerical modeling of packed-bed thermal energy storage systems. *Sol. Energy* **2017**, *153*, 628–654. [CrossRef]